MASTER THESIS

Numerical Simulation of non-Newtonian Fluid-Structure Interaction Problems

Ahmad AMANI

Director:
Prof. Assensi OLIVA

ETSEIB

Escola Técnica Superior
d'Enginyeria Industrial de Barcelona

UPC

Declaration of Authorship

I, Ahmad AMANI, declare that this thesis titled, “Numerical Simulation of non-Newtonian Fluid-Structure Interaction Problems” and the work presented in it are my own. I confirm that:

- This work was done wholly or mainly while in candidature for a research degree at this University.
- Where any part of this thesis has previously been submitted for a degree or any other qualification at this University or any other institution, this has been clearly stated.
- Where I have consulted the published work of others, this is always clearly attributed.
- Where I have quoted from the work of others, the source is always given. With the exception of such quotations, this thesis is entirely my own work.
- I have acknowledged all main sources of help.
- Where the thesis is based on work done by myself jointly with others, I have made clear exactly what was done by others and what I have contributed myself.

Signed:

Date:

Now this is not the end.
It is not even the beginning of the end.
But it is, perhaps, the end of the beginning.

“Winston Churchill”

UNIVERSITAT POLITÉCNICA DE CATALUNYA

Abstract

Escola Técnica Superior
d'Enginyeria Industrial de Barcelona

Master of Science

Numerical Simulation of non-Newtonian Fluid-Structure Interaction Problems

by Ahmad AMANI

This thesis represents a numerical method to solve fluid-structure interaction (FSI) problems where the fluid exhibits a non-Newtonian behavior. Oldroyd-B constitutive equations is used to model Viscoelastic fluid and Generalized Newtonian Fluids are used to model Shear-thinning/Shear-thickening fluids. For FSI solution, a semi-implicit partitioned method is used which separates the fluid pressure term and strongly couples it to the structure, while the remaining fluid terms are only weakly coupled. Numerical tests provides information regarding the physical behaviour of the fluid and structural response of the elastic domain in non-Newtonian fluid-structure interaction problems.

Acknowledgements

I would like to express my deep gratitude to Professor Assensi Oliva, for giving me the opportunity to do this study as well as his patient guidance, enthusiastic encouragement and useful critiques of this research work.

I am particularly grateful for the assistance given by Dr. Deniz Kizildag who helped me a lot in different stages of this master program.

Assistance provided by Mr. Alireza Naseri is greatly appreciated.

. . .

Contents

List of Figures

List of Tables

List of Abbreviations

VF	**V**iscoelastic **F**luid
FSI	**F**luid **S**tructure **I**nteraction
NFSI	**N**ewtonian **F**luid **S**tructure **I**nteraction
VFSI	**V**iscoelastic **F**luid **S**tructure **I**nteraction
STF	**S**hear **T**hickening **F**luid
SThinningF	**S**hear **T**hinning **F**luid
GNF	**G**eneralized **N**ewtonian **F**luid
Wi	**W**e**i**ssenberg Number
HWNP	**H**igh **W**eissenberg **N**umber **P**roblem
BSD	**B**oth **S**ides **D**iffusion
PDPS	**P**ositive **D**efiniteness **P**reserving **S**cheme
LCR	**L**og **C**onformation **R**epresentation
SRCR	**S**quare **R**oot **C**onformation **R**epresentation
SVF	**S**tandard **V**iscoelastic **F**ormulation

List of Symbols

d	Diameter	m
ρ	Density	$\mathrm{kg/m^3}$
μ	Dynamic Viscosity	$\mathrm{kg/(ms)}$
μ_0	Zero Shear Dynamic Viscosity	$\mathrm{kg/(ms)}$
μ_∞	Infinite Shear Dynamic Viscosity	$\mathrm{kg/(ms)}$
ν	Kinematic Viscosity	$\mathrm{m^2/s}$
$\dot{\gamma}$	Shear Rate	$\mathrm{s^{-1}}$
τ	Shear Stress	$\mathrm{kg/(ms^2)}$
λ	Relaxation time	s
β	Retardation Ratio	-
$\mathbf{c}$	Conformation Tensor	-

To my family and Dr. Fang Su
Although they still have no idea what I do…

Chapter 1

Introduction

1.0.1 Fluid-Structure Interaction Problems

Fluid-structure interaction (FSI) problems include a fluid flow mutually interacting with a moving or deforming structure. Fluid flow exerts surface forces on the solid's wet boundary and the movement of the structure alters the fluid's motion. There is a wide range of applications cited for FSI, from civil to biomedical engineering. An interesting example of FSI application in biomedical engineering is simulation of blood flow inside deformable vessels in human arteries. The simulations help on shedding light on the flow of blood inside the vessels and improving the quality of artificial blood vessels and predicting the rupture of aneurysms during specific medical treatments [1, 2]. To have a more clear understanding of the importance of studies in the field of fluid-structure interactions, the case of aneurysms treatment will be discussed in details:

An aneurysm is an abnormal localized enlargement of a portion of an artery, resulted of the weakness in the wall of the blood vessel. The relative fatality rate is unusually high: when the thoracoabdominal aneurysms (TAs) approaches the size of d=6–10 cm or more, in 62% of the cases it leads to rupture or dissect [3]. In these cases, according to Elefteriades [4], the surgical interferences are suggested for aneurysms with the size of d=0.5 cm below the critical diameter. However, surgical repairs of TA are hazardous and expensive. According to Culliford et al. [5] operating on patients with ruptured or dissected aneurysms leads to the death of at least 15% of the patients; moreover, surgical treatment of aneurysms have serious disadvantages, e.g. paraparesis or paraplegia in 4.6% of the cases. Furthermore, Vorp et al. [6] has suggested that the failure of an ascending thoracic aneurysm wall is not linked to its diameter. Using numerical simulations of patient-specific geometry, however researchers are able to perform patient-specific wall stress analysis to provide further information on the role of anatomical features such as the shape and wall composition on the stress pattern and consequently the potential rupture of thoracic aneurysms [2].

Another exciting application of fluid-structure-interaction problems is predicting the flow and wake induced vibration which has a wide range of applications in engineering e.g. the submerged structures in offshore equipment [7]. Over the past decades, flow and wake induced oscillations have gained growing interests from both the scientific and practical communities.

Wake induced vibration can occur when long and flexible objects are immersed in the flow field, they will be excited to vibrate by the external forces from the flow that passes by. Meanwhile, the movements of the cylinders will in return change the flow features and characteristics. If there is only one object freely oscillating in the flow field, usually recognized flow patterns including “2P”, “2S” and “P+S” (where “P” stands for a pair of vertices, and “S” means one) can be found for different parameter settings. Meantime, the “lock-in” or “lock-on” performance may appear meaning that as the vortex shedding frequency approaches its natural frequency, the cylinder experiences a vibration with relatively high amplitude.

Another case of flow induced vibration is when there are two (or more) bluff bodies (for example circular cylinders) dominated by a cross flow with one of them placed downstream in the wake of the other object. This framework is common, for example, in the cases of overhead electric power transmission lines subjected to the wind, clustered offshore risers under the effect of ocean currents, bridges and heat exchangers, to name a few. In these cases a pattern as shown in 1.1 is frequently witnessed in the flow trajectory of the cylinder movement specially in the ocean platform systems. More details about flow induced oscillations could be found in review work of Williamson and Govardhan [8].

Wake induced vibrations are the strongest for the in-line composition. For this arrangement, the downstream body is placed entirely behind the upstream body along the flow direction. However, the complete mechanism of wake-induced vibration is yet to be discovered [10]. According to Paidoussis, J. Price, and Langre [10], the downstream body can oscillate transversely with an excessive peak-to-peak amplitude of 10D. These vibrations

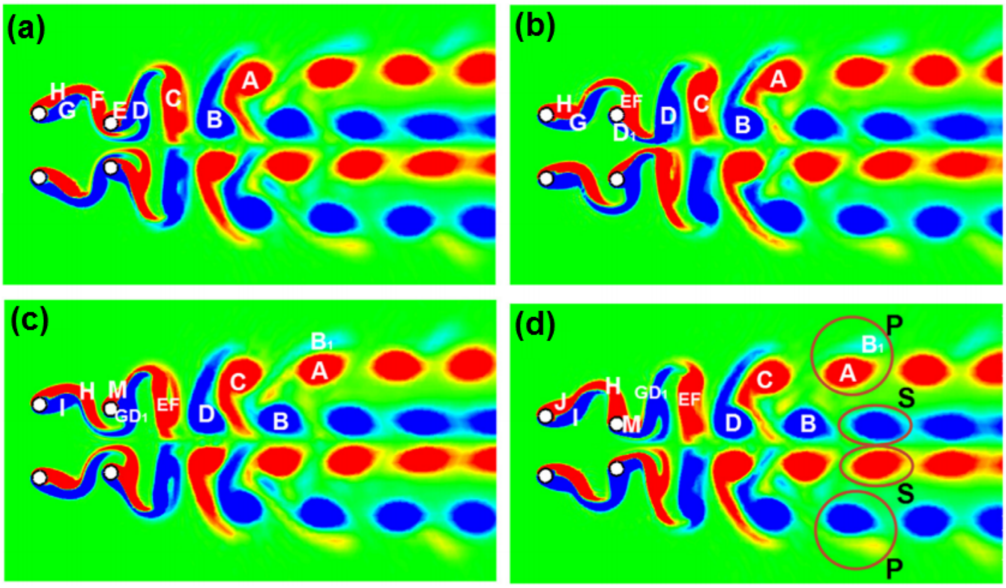

FIGURE 1.1: Evolution of vorticity for fluid induced vibration of four circular cylinders [9].

can cause significant structural damages due to fatigue and thus impose severe concerns in engineering applications.

Experiments and numerical simulations are widely used in studying the flow induced vibration problems. In most of the experimental works, the flow parameters including Reynolds number are in the turbulent flow regime and limited. Contrary, the flexibility of numerical simulations on implementing different initial conditions, boundary conditions and fluid properties, as well as their capability to extract substantial information on the flow field, makes them extra appealing on studying these problems. Numerical simulations of flow induced vibrations can provide significant details on the nature of the problem, e.g. oscillation analysis of the structure, structural fatigue, velocity and vorticity fields which are difficult or impossible to capture experimentally or analytically. As a result, significant attention is given to numerical simulations of flow induced vibration problems [11, 12].

Now that important aspects of numerical simulation of fluid structure interaction problems are discussed, we are going to review the approaches in solution of these problems.

Generally, two different strategies are widely used to solve FSI problems, namely monolithic and partitioned methods. In monolithic approach, a single solver is used to solve the governing fluid and structure equations simultaneously. Since these equations are solved concurrently, the interaction between the fluid and structural domains is inherently taken into account. The main advantage of the monolithic approach is that there would be no need for any extra coupling procedures between fluid and structure interface which reduces the complexity of the original problem. Nevertheless, this technique demands to apply the same numerical methods in discretization and solution of the fluid and structural equations. However, the fluid and structural governing equations are different and specific considerations have to be taken into account for each of them separately. As a result, the monolithic methods are reported to be less efficient or reliable in some applications [13]. Another disadvantage of the monolithic approach is its inability to employ the already-developed fluid and structural solvers. Therefore, it requires an extensive numerical programming effort which generally leads to a less modular solver [13, 14].

partitioned methods, on the other hand, employ separate solvers for fluid and structural equations and utilize a coupling scheme to consider the interaction of the domains. The coupling scheme resolves the order and frequency in which the fluid and structural equations need to be solved. Moreover, It determines the communication technique and information exchange between the two solvers. This information exchange is primarily bounded to the fluid-structure interface. Partitioned approaches mitigate both mentioned disadvantages of the monolithic schemes. It enables utilizing the most suitable numerical methods for each sub-problem, e.g. fluid problem and structural problem. Each of these methods for solving the sub-problems could previously be tested and verified on numerous cases which significantly increases the reliability of the numerical simulations. It also allows the application of the previously developed solvers for fluid and structural equations separately which reduces the required development effort and increases the modularity of the solvers. Despite the mentioned advantages, the partitioned approaches append a new challenge to the problem, i.e. the coupling technique required in the interface between the two solvers [13, 14].

Partitioned methods are further divided into two categories of explicit (loosely coupled) and implicit (strongly coupled) schemes. In an explicit coupling method, the fluid and structural equations are solved only once and in a sequence at every timestep. As a result, explicit methods do not satisfy the exact coupling condition at the fluid–structure interface. In this sub-category, the most basic explicit scheme is the conventional serial staggered method [15]. Contrary, Implicit methods, enforce the equilibrium condition at the interface through coupling iterations between the fluid and structural solvers at each time step. Two most commonly used techniques to accomplish the FSI coupling iterations are Fixed-point (Gauss–Seidel or Jacobi) iterations [13, 16] and Newton-based methods [17, 18, 19]. Besides them, vector extrapolation methods have also been used for this end [16].

Explicit methods perform correctly for aeroelastic problems concerning compressible flows [15, 20]. Nevertheless, they are unstable for a wide range of problems, particularly incompressible flow problems and low solid/fluid density ratios ($\rho_m/\rho_f \approx 1$). This instability is regardless of the time step or discretization schemes of the governing equations of each domain. It is inherent to the coupling method named "the added-mass effect". The instability arises since fluid forces in the explicit coupling depend on a predicted displacement of the structure, rather than the correct one. As the structure moves, it ought to accelerate the bulk of the fluid around it as well. Consequently, part of the fluid acts as an extra mass in the structural dynamics system, causing the added-mass effect. This effect is especially strong when densities of the fluid and the structure are alike. For any loosely coupled method, there is a density ratio limit in which the method experiences instability beyond it [21, 22]. While added-mass effect causes instability in the loosely coupled schemes, it deteriorates convergence of the strongly coupled methods. Hence, an FSI problem with strong added-mass effect is also challenging for implicit methods, as it requires many coupling iterations in order to converge at each time step [21, 22].

Implicit methods provide a stable solution for FSI problems with strong added-mass effect, of which explicit methods are not capable. However, significantly higher computational resources are required as several iterations of solving the complete system of governing equations many times per time step are needed. To mitigate this deficiency, Fernández and Moubachir [18] introduced a semi-implicit coupling technique in which they used a projection method to solve the fluid equations and only implicitly coupled the projection step with the structure. Consequently, the pressure stress term of the fluid has strongly coupled with the structure. According to Causin, Gerbeau, and Nobile [21], the pressure stress term is the main contributor to the added-mass effect and coupling this term explicitly causes numerical instability. With implicit treatment of the pressure stress added-mass term, the semi-implicit method maintains the promising stability of the implicit schemes, while explicit treatment of the other terms helps to avoid excessive computational cost [18]. A very similar method was suggested by Breuer and Münsch [23] to solve FSI problems in turbulent flows. A similar approach is presented in the hybrid monolithic-partitioned method of Grétarsson, Kwatra, and Fedkiw [24] for FSI problems with compressible flows which strongly couples the fluid pressure and structure velocity by solving them implicitly in a monolithic way, while the remaining terms are loosely coupled in a partitioned manner. Other semi-implicit methods are also reported in the literature which share the same basic idea. The reader is recommended to refer to [25, 26] and [27] for more details.

Despite receiving attentions from researchers in the past decade, semi-implicit coupling methods are far from maturity. Most of the reported methods lack modularity and simplicity and are only tested in a few ranges of specific FSI problems and their robustness in solving different types of FSI problems is yet to be evaluated.

1.0.2 Non-Newtonian Fluids

Newtonian fluids are named after Issac Newton which first described the flow characteristics of fluids with a simple linear relation between shear stress τ and shear rate $\dot{\gamma}$. This relation is known as Newton's Law of Viscosity, where the proportionality constant μ is the viscosity of the fluid as:

$$\tau = \mu \times \dot{\gamma} \tag{1.1}$$

where τ is the local shear stress of the fluid, $\dot{\gamma}$ is the local shear rate of the fluid, and μ is the viscosity of the fluid. Some examples of Newtonian fluids include water and air, in which their viscosity is only a function of temperature. Newtonian fluids are usually constituted of small isotropic molecules, symmetric in shape and properties, which are not oriented by the flow field. However, it is also feasible to witness Newtonian behaviour in large an-isotropic molecules e.g. low concentration proteins which they might show a constant viscosity regardless of flow field's shear rate.

In reality, however, most of the fluids are showing non-Newtonian behaviour, meaning their viscosity is dependent on shear rate or the deformation history. Non-Newtonian fluids can display either a non-linear relation between shear stress and shear rate, can have yield stress or viscosity that is dependent on deformation history or a combination of them.

In this work, we will study three types of non-Newtonian shear-thinning/ shear-thickening/ Viscoelastic fluids interacting with structure. For this reason we will briefly review the notion and pioneering works in each of these fields.

Shear-Thinning Fluids

The most common type of time-independent non-Newtonian fluids are shear-thinning (or pseudoplastic), in which their apparent viscosity decreases with increasing shear rate. In these types of fluids, however, both at very low and very high shear rates, Newtonian behaviour is observed, meaning shear stress is having a linear relation with shear rate. The values of the apparent viscosity at these very low and high shear rates are known as the zero shear viscosity, μ_0, and the infinite shear viscosity, μ_∞.

Figure 1.3 illustrates the variation of apparent viscosity along with μ_0 and μ_∞ as a function of shear rate ($\dot{\gamma}$) for a shear-thinning fluid. The order of changes in the shear rate and apparent viscosity for this case are very wide. According to Chhabra and Richardson [28], shear rates associated to μ_0 and μ_∞ viscosities are dependent on several parameters, including the type and concentration of polymer, the molecular weight distribution and the nature of its solvent, making it difficult to present a valid generalizations. However, many materials exhibit their μ_0 and μ_∞ at shear rates below $10^{-2}\ s^{-1}$ and above $10^5\ s^{-1}$ respectively. When the molecular weight of the polymer decreases, since its molecular weight distribution becomes restricted, and its polymeric concentration in solution declines, the range of shear rate where $\mu = \mu_0$ (apparent viscosity is constant in the zero-shear region) increases [28].

Utilizing the Generalized Newtonian Fluid (GNF) formulation for modeling the shear-thinning and shear-thickening fluids is very common among researchers to represent the rheology of this types of fluids. However, some cares must be taken into account. The

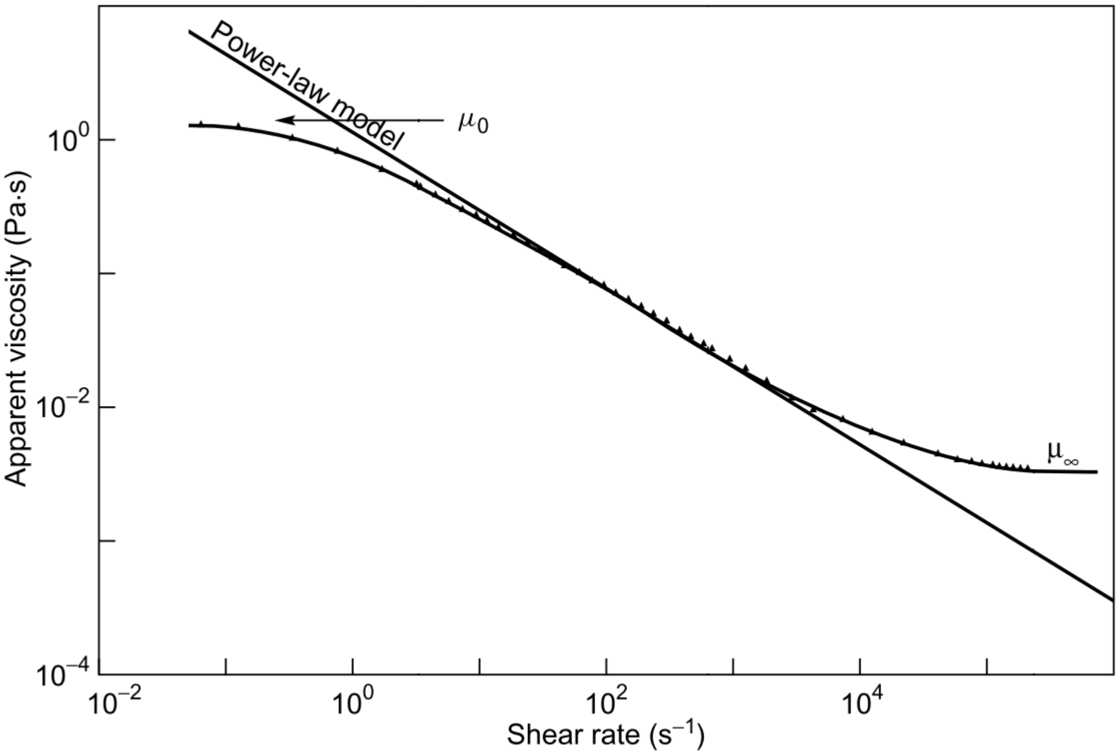

FIGURE 1.2: Illustration of μ_0 and μ_∞ for a Shear-Thinning fluid

possibility of its usage in fluid flows other than simple shear is not straightforward. Consequently, in these cases, the numerical models should be verified by experimental results. On the other hand, GNF constitutive equation is unable to predict the normal shear stresses, which are elastic effects. As a result, GNF constitutive equations are mainly suitable and accurate for flows in which the elastic effects are negligible. Besides, in the GNF models, the history of deformation is not taken into account which is not proper for materials with memory. Therefore, the GNF models could successfully be applied to fluids in which represent notable shear-rate dependent viscosity, but negligible small normal stress differences or fluids in which the effect of a variable shear viscosity is dominant compared to the normal stresses [29].

Various mathematical formulations with diverse complexity and types have been suggested by researchers to model shear-thinning features. Some of these attempts are concerned with curve fitting of the available experimental data, providing empirical relationships for the shear stress–shear rate curves. On the other hand, other attempts have theoretical basis in statistical mechanics. In this research, we discuss a selection of the most common viscosity models. The reader is refereed to Bird [30] for a more comprehensive analysis of the available models.

- The power-law or Ostwald de-Waele model:

  This model is one of the most widely used formulation to characterize shear-thinning fluids, among the researchers. In this model, the relationship between shear stress (τ) and shear rate ($\dot{\gamma}$) could be approximated by a formulation of following over a limited range of shear rate.

  $$\tau_{yx} = m\dot{\gamma}_{yx}^{n} \tag{1.2}$$

  Consequently, the apparent viscosity of this model would be as:

  $$\mu(\dot{\gamma}) = \tau_{yx}/\dot{\gamma}_{yx} = m\dot{\gamma}_{yx}^{n-1} \tag{1.3}$$

  where **m** and **n** are empirical curve-fitting parameters named fluid consistency coefficient and the flow behaviour index, respectively. note that for **n=1** the model exhibits Newtonian behaviour. Even though this model offers a simple representation of shear-thinnig fluids, it has disadvantages. One is the parameters **m** and **n**, are not entirely constant and are dependent on the value of shear rate $\dot{\gamma}$. Another problem of this model could be seen in figure 1.2, as it does not predict the zero and infinity shear viscosities (μ_0 and μ_∞).

- The Carreau viscosity equation:

  In order to overcome the shortcoming of power-law model in deviation at very high and very low shear rates, Carreau [31] proposed a model based on the molecular network considerations, which incorporates limiting viscosities of μ_0 and μ_∞ as follow:

$$\frac{\mu - \mu_\infty}{\mu_0 - \mu_\infty} = \left(1 + (\lambda \dot{\gamma}_{yx})^2\right)^{(n-1)/2} \tag{1.4}$$

In this formulation, the parameters **n**(<1) and λ are empirical curve-fitting parameters. For either λ or **n** equal to zero and $\mu = \mu_0$ the model predicts a Newtonian fluid behaviour.

In this work we use the discusses model of 1.2 to simulate the shear-thinning fluids.

Shear-Thickening Fluids

Shear thickening is defined in the British Standard Rheological Nomenclature as the increase of viscosity with increase in shear rate. The shear-thickening behaviour of fluids had been an important topic of interest for rheologists over the last two decades. The term shear-thickening is usually used to refer to fluids in which dynamic viscosity increases as the applied shear rate has risen. The phenomenon is frequently encountered in various industries [32]. The onset of shear-thickening marks the point when hydrodynamic interactions begin to predominate in the system. However, the microstructural basis for this behaviour remains unresolved. Hoffman [33], in his pioneering studies, used a combination of rheology with *in situ* light diffraction to clarify microstructural variations that happen during shear-thickening. He concluded that the incipience of shear-thickening at a critical shear rate ($\dot{\gamma}$) corresponds to a transition from an easy flowing status where the particles are organized into layers to a disordered state where this ordering is absent. This mechanism is commonly called an *order-disorder transition*. Researchers have been studying to answer this question: whether an order-disorder transition indeed takes place in all shear-thickening fluids. Stokesian dynamics simulations done by Bossis and Brady [34] and Brady and Bossis [35] have shown that clusters of particles characterize the shear-thickened state. The formation of these flow-induced clusters leads to an increase in the energy dissipation, and as a result, the viscosity increases. Hence, according to Bossis and Brady [34] and Brady and Bossis [35], shear-thickening is not related to the elimination of ordered layers but the generation of particle clusters. However, under certain conditions, both events may co-occur (i.e., the disruption of the ordered layer structure can be caused by the clustering of particles). Nevertheless, for the clustering theory to hold, the existence of an ordered state before the shear-thickening transition is not necessary.

Because of its specific characteristics, shear-thickening fluids are used widely in different engineering applications, e.g. energy absorbers, vibration controllers and safety protects [36, 37, 38, 39, 40, 41, 42, 43, 44]. For instance, Petel et al. [38] studied the effect of the particle strength and volume fraction on the deceleration performance of STF. Lu et al. [43] studied the compressive behaviour of warp-knitted fabrics impregnated with shear-thickening fluids. Park et al. [42] experimentally and numerically investigated the absorption characteristics of Kevlar fabrics impregnated by shear-thickening fluids at a velocity of $V \approx 1-2km/s$.

Another current investigation being performed is related to the integration of STFs into composite structures. Tan et al. [41] investigated the energy absorption features of a sandwich plate with a shear-thickening fluids core subjected to penetration loading. Fischer et al. [44] reported the effect of a shear-thickening fluid core on the vibration suppression of a sandwich beam. Since these composite sandwich structures tune their part stiffness and damping capacity under dynamic deformation, they may be used in ski boards pursuing the absorption of vibrations, what would lead to increase the comfort and the control of the skier, reducing also the possibility of joint injuries.

Similar to what happens in some electro-rheological and magneto-rheological fluids, stabilized concentrated colloidal suspensions of rigid nanometric particles in a carrier fluids exhibits shear thickening behaviour exclusively under mechanical deformation and without the necessity of an external power source. which could help in vibration control using STFs [45]. Nevertheless, shear thickening is an unwanted behaviour in many other cases and since this could lead to technical problems and even to the destruction of equipments like pumps or stirrers, special care should be taken into account in the design process of devices with STFs [46]. Figure 1.3 schematically represents the shear-stress as a function of shear-rate for Newtonian/Shear-Thickening/Shear-Thinning fluids discussed in this section.

Shear-thickening fluids exhibit three characteristics regions:

- Region **a**, where a minor shear-thinning behaviour exists up to a critical shear rate ($\dot{\gamma}_c$).

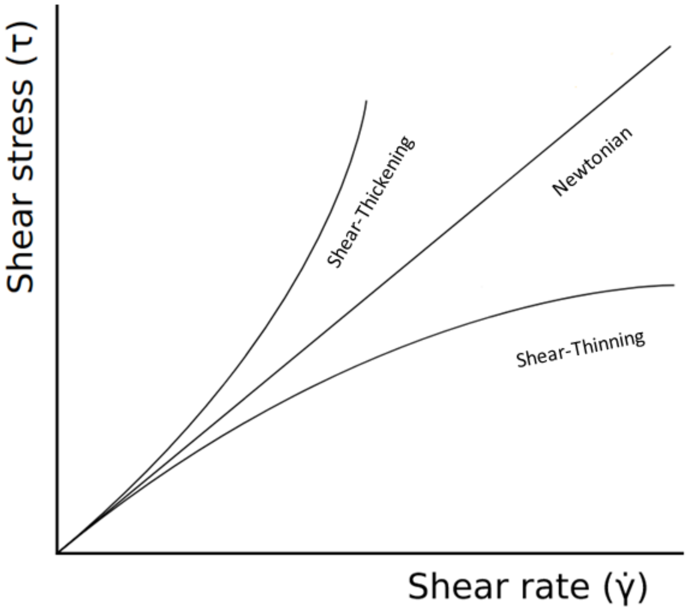

FIGURE 1.3: Shear stress as a function of shear rate for Newtonian/Shear-Thickening/Shear-Thinning fluids.

- A relatively wide region **b**, in which shear-thickening happens. This shear-thickening takes place between two values of $\dot{\gamma}_c$ and a higher critical value $\dot{\gamma}_{max}$, where the apparent viscosity is maximum.

- Region **c** by an abrupt shear thinning behaviour for values of $\dot{\gamma} > \dot{\gamma}_{max}$

These regions are schematically depicted in figure 1.4.

Various formulations have been developed and applied as Generalized Newtonian Fluid models for the case of shear-thinning fluids. Contrary, for shear-thickening fluids, despite the considerable amount of works in the literature devoted to microscopic models, it is prevalent to model the shear-thickening fluids utilizing the simple power-law model as described in section 1.0.2, equation 1.2 for **n** values greater than 1. Although the power-law constitutive equation can successfully model the shear rates intervals where the viscosity increases with the shear rate (**n** > 1), it fails to predict the low and high shear rate regions, where shear-thinning behaviours are normally observed [47].

An efficient approach to tackle this problem is to use a piecewise definition to take the mentioned three different regions into account separately. Different piecewise functions

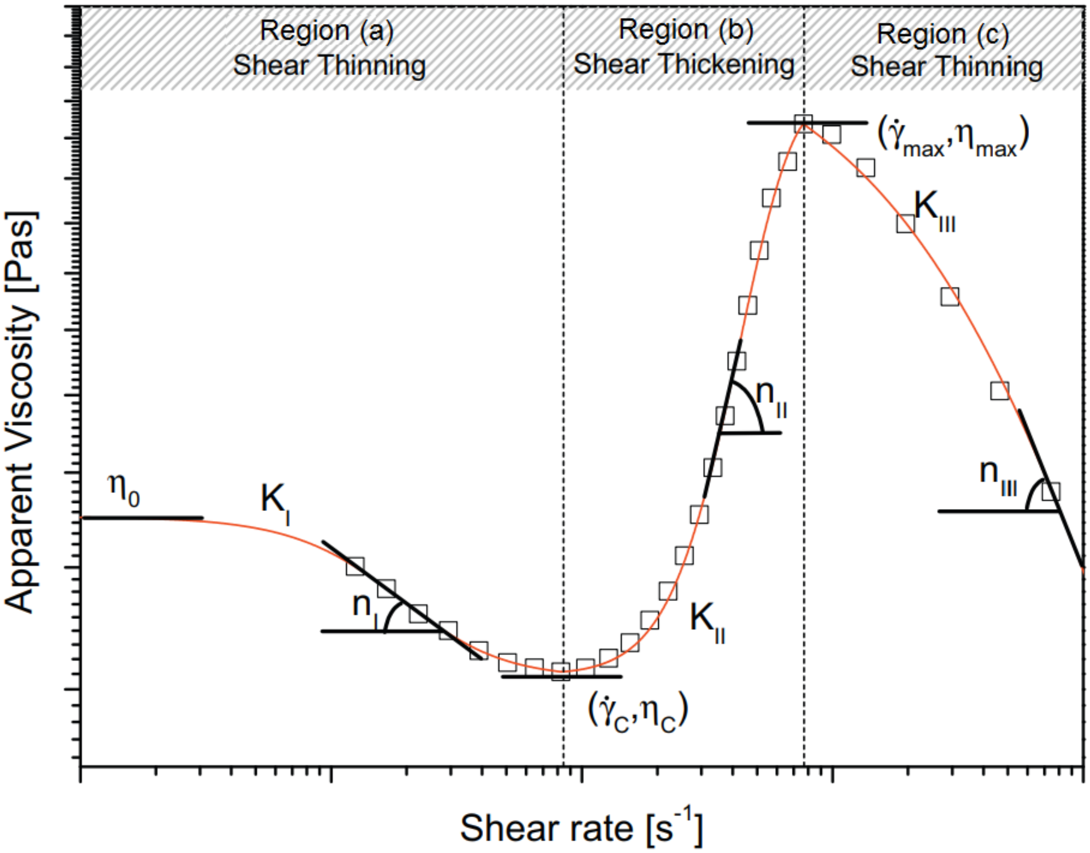

FIGURE 1.4: Conventional viscosity curve of a shear thickening-fluid

are suggested by researchers in the literature for shear-thickening fluids. Among all of them, the model proposed by Galindo-Rosales, Rubio-Hernández, and Sevilla [48] has drawn significant attention in the scientific comunity. In this model the apparent viscosity is described as below:

$$\mu(\dot{\gamma}) = \begin{cases} \mu_I(\dot{\gamma}) = \mu_c + \frac{\mu_0-\mu_c}{1+\left[\lambda_I\left(\frac{\dot{\gamma}^2}{\dot{\gamma}_c-\dot{\gamma}}\right)\right]^{n_I}}, & \dot{\gamma} \leq \dot{\gamma}_c. \\ \mu_{II}(\dot{\gamma}) = \mu_{max} + \frac{\mu_c-\mu_{max}}{1+\left[\lambda_{II}\left(\frac{\dot{\gamma}-\dot{\gamma}_c}{\dot{\gamma}_{max}-\dot{\gamma}}\right)\dot{\gamma}\right]^{n_{II}}}, & \dot{\gamma}_c < \dot{\gamma} \leq \dot{\gamma}_{max}. \\ \mu_{III}(\dot{\gamma}) = \frac{\mu_{max}}{1+[\lambda_{III}(\dot{\gamma}-\dot{\gamma}_{max})]^{n_{III}}}, & \dot{\gamma}_{max} < \dot{\gamma}. \end{cases} \tag{1.5}$$

The model parameters are usually determined from simple shear flow data [48]. In this equation, λ_i parameters are positive characteristic time constants. In this work we use this model to simulate the shear-thickening fluids.

Viscoelastic Fluids

In the classical elasticity theory, the stress is proportional to the strain. For tension, Hooke's law applies and the mentioned coefficient of proportionality is known as Young's modulus, G. If an elastic solid is deformed, after the stress is being removed, it regains its original form. Although, if the applied stress surpasses the characteristic yield stress of the material, the deformed solid will not face full restoration and a phenomenon called *creep* will happen.

On the other hand, as discussed before, in a Newtonian fluid, the shear stress is proportional to the shear rate. Many materials show both elastic and viscous behaviours under given circumstances. These materials are said to be viscoelastic. Ideal elastic deformation and ideal viscous flow are in fact, extreme cases of viscoelastic behaviour. For a wide range of materials, mainly these extreme conditions are observed, e.g. the elasticity of water and the viscosity of ice are usually unnoticed.

Various materials including polymer melts, polymer and soap solutions, synovial fluid and etc., present viscoelastic behaviour. These materials can store and recover shear energy, as viscous liquid energy is dissipated, but elastic solid energy is recoverable. Many strange phenomena have been witnessed in viscoelastic fluids, e.g. die swell, rod climbing or Weissenberg effect, tubeless siphon, negative wake of rising bubbles and the development of secondary flows at low Reynolds numbers. Figure 1.5 illustrates the two phenomena of die-swell and negative wake observed in viscoelastic fluids. The reader is reffered to Bird [30] and Carreau [31] for more details on behaviour of viscoelastic fluids.

As mentioned before, in viscoelastic materials, the stress response does not only depend on their current deformation but also on their deformation history. Therefore, time is a crucial parameter in understanding the viscoelastic materials. Viscoelastic materials usually show stress relaxation, creep deformation and shape memory.

Viscoelastic behaviour of fluid is prevalent in a wide range of applications including food processing, pharmaceuticals, casting industry and chemical industry [49]. One of the important applications of Viscoelastic fluids is in microfluidic devices, for instance memory and control devices [50] and microfluidic rectifiers [51], use Viscoelastic materials as working fluid. A huge portion of biological fluids in nature exhibit viscoelastic behavior.

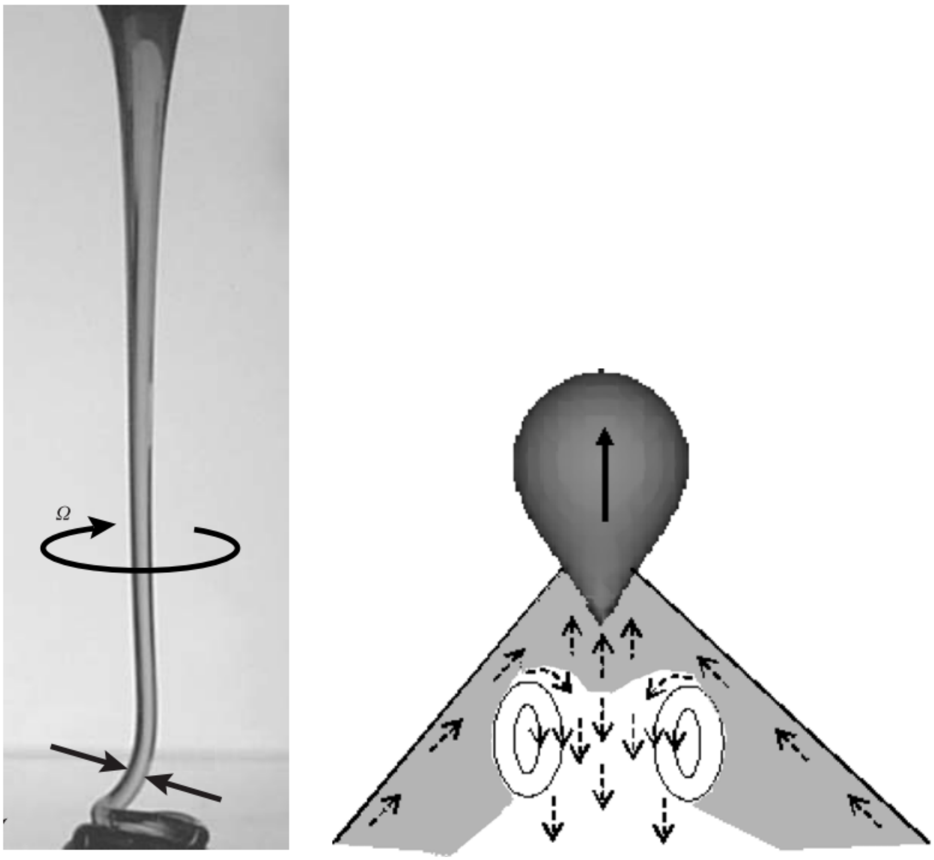

FIGURE 1.5: Left: die swell phenomena observed in viscoelastic fluids, Right: negative-wake and cusp-shaped trailing edge of gas bubble rising in viscoelastic fluids.

Thus it is important to understand the dynamics of Viscoelastic fluids. Numerical simulation has become a powerful method in studying the underlying physics of viscoelastic behaviour of the fluid and also an important tool in design and manufacturing process of Viscoelastic applications. In numerical simulations, the Viscoelastic flow is solved using Navier-Stokes equations integrated with an extra constitutive equations which describes the relation of stress with strain rate tensor [52]. A variety of numerical methods, including finite difference, finite element, finite volume and hybrid methods, have been developed to simulate viscoelastic flows [53, 54, 55, 56].

The relative effect of viscoelasticity is usually quantified by either one of the dimensionless *Weissenberg* number or dimensionless *Deborah* number. Weissenberg number is the ratio of elastic forces to viscous forces and is formulated as product of characteristic relaxation time λ and shear rate. Deborah number is mainly used in flows with a non-constant stretch history, and physically represents the rate at which elastic energy is stored or released. It is defined as the ratio between the characteristic relaxation time and the time scale of observation:

$$Wi = \lambda\dot{\gamma} \tag{1.6}$$

$$De = \lambda/t_{scale} \tag{1.7}$$

Continuum constitutive equations for viscoelastic fluids could be driven from the kinetics theories. In most numerical simulations of practical applications concerning viscoelastic fluids, however, the constitutive model and the material properties are extracted from rheological experiments. Many of the conventional constitutive models can predict un-physical characteristics, called constitutive instabilities. They can be categorized into two classes: the Hadamard instability and the dissipative instability [57]. The Hadamard instability is referred to as the elastic response under sudden or high-frequency wave distributions. The dissipative instability is referred to as boundless free energy or rate of energy dissipation with increasing deformations. As a result, special care must be taken into account to find proper constitutive models. In constitutive models extracted from molecular theories, the stress response to the deformation of the fluid, τ, is decomposed into two parts of solvent (τ_s) and polymerice (τ_p) stresses, which corresponds to the instantaneous response of the solvent, and time-dependent contribution of the polymer ($\tau = \tau_s + \tau_p$). In this formulation $\tau_s = 2\mu_s\dot{\gamma}$ and $\tau_p = G_0 f_s(\mathbf{c})$, where $\mu_s = \beta\mu_0$ is the solvent viscosity, $G_0 = (1-\beta)\mu_0/\lambda$ is the plateau elastic moduli, $f_s(\mathbf{c})$ is the strain function determined by the constitutive formulation, μ_0 is the steady-state viscosity and β is the retardation ratio or solvent viscosity ratio. Conformation tensor $\mathbf{c}$ is an internal tensor variable representing the macro-molecular configuration of the polymeric chains. The conformation tensor is a second-order internal structural tensor correlated with the second moment of the chain end-to-end distribution function. According to Beris and Housiadas [58], the eigenvalues of this tensor have the physical meaning of the square of the average macromolecular size along the principle three directions and their corresponding eigenvectors have the physical meaning of the orientation of those directions in space. As a result of their physical meaning, all those eigenvalues need to be positive, i.e. the conformation tensor needs to be positive definite. Although on the continuum space, the conformation tensor remains positive definite as it evolves in time, on the discretised space this may not happen. An improper discretisation of the constitutive equation of viscoelastic fluid can ignore this property, leading to numerical instability. Figure 1.6 illustrates the molecular topology of polymeric chain in different constitutive models of FENE, PTT, Rolie-Poy and XPP models.

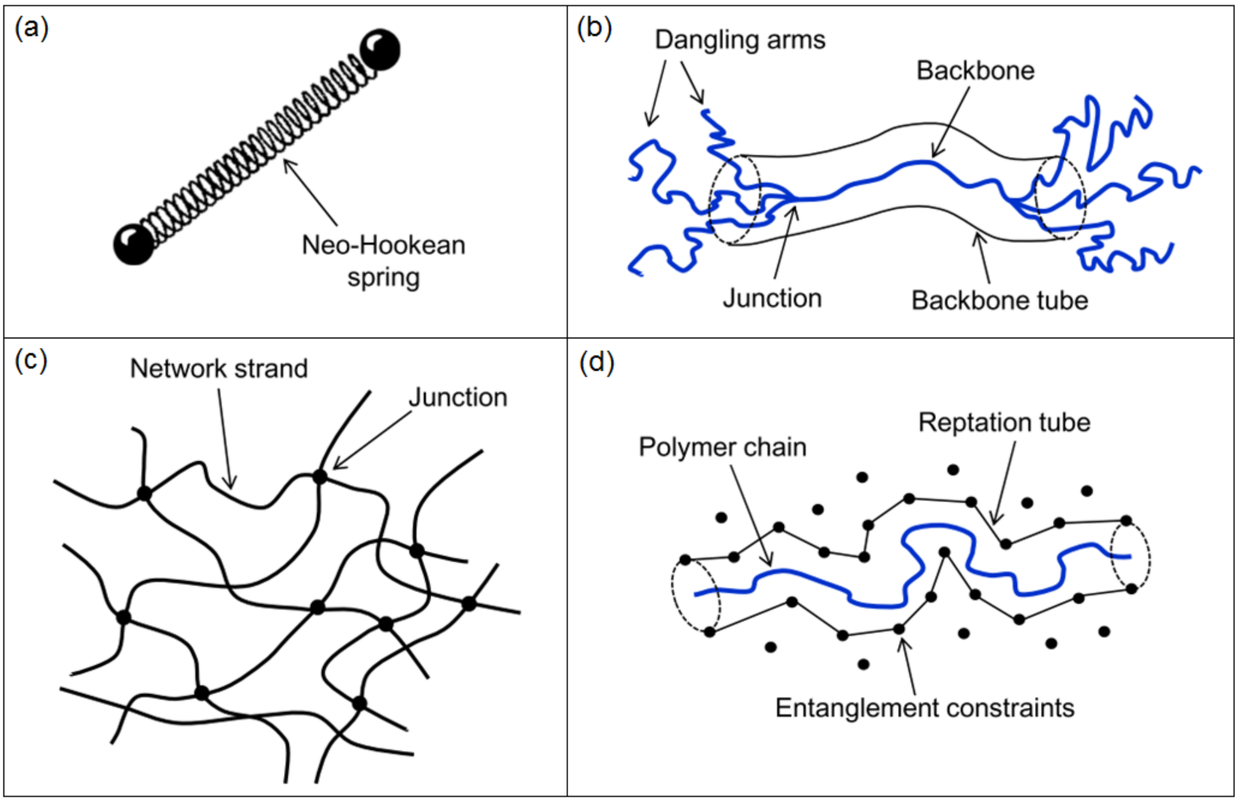

FIGURE 1.6: Molecular topology in different constitutive models: (a) Dumbbell molecule in the FENE model (b) Pom–Pom molecule in the XPP model (c) Polymer network in the PTT model (d) Entangled linear polymer in the Rolie–Poly model

The conformation tensor is by definition a symmetric positive definite tensor, in which is equal to the identity matrix $\boldsymbol{I}$ while the polymeric chain is at the equilibrium state. A

TABLE 1.1: Summary of the strain and relaxation functions for most popular constitutive formulations of viscoelastic fluids, derived from molecular theories.

Name	$f_s(\mathbf{c})$	$f_R(\mathbf{c})$
Oldroyd–B	**c-I**	**c-I**
Giesekus	**c-I**	$\alpha\mathbf{c}^2+(1-2\alpha)\mathbf{c}-(1-\alpha)\mathbf{I}$
FENE–CR	$\frac{\mathbf{c}\text{-}\mathbf{I}}{1-tr(\mathbf{c})/L^2}$	$\frac{\mathbf{c}\text{-}\mathbf{I}}{1-tr(\mathbf{c})/L^2}$
FENE-P	$\frac{\mathbf{c}}{1-tr(\mathbf{c})/L^2}-\mathbf{I}$	$\frac{\mathbf{c}}{1-tr(\mathbf{c})/L^2}-\mathbf{I}$

differential equation governs the primary mechanism of stress build-up and stress relaxation concerning the conformation tensor as:

$$\overset{\nabla}{\mathbf{c}}=-\frac{1}{\lambda}f_R(\mathbf{c}) \tag{1.8}$$

In this formulation, $^\nabla$ is the upper-convected time derivative operator, which for and arbitrary tensor of **A** is defined as:

$$\overset{\nabla}{A}=\frac{\partial A}{\partial t}+u.\nabla A-\nabla u^T.A-A.\nabla u \tag{1.9}$$

In equation 1.8, $f_R(\mathbf{c})$ is a relaxation function defined according to the constitutive model. In the constitutive models based on molecular theories, the strain and relaxation functions of, $f_s(\mathbf{c})$ and $f_R(\mathbf{c})$, are polynomials functions of the conformation tensor in which their coefficients can depend on the first, second and third invariants of **c**. The strain and relaxation functions are usually first and second-order polynomials, respectively.

Table 1.1 represents a summary of the strain and relaxation functions for most popular constitutive formulations of viscoelastic fluids, derived from molecular theories. In the formulations in this table, ***tr(c)*** stands for the trace of **c** as it is equal to its first invariant.

- The *Oldroyd–B* model which is also called *contravariant convected Jeffreys model*, was initially introduced by Oldroyd [59]. It was the first material frame-invariant phenomenological model describing viscoelastic fluids.

- The *Giesekus* model proposed by Giesekus [60] includes quadratic terms of the stress, which can be interpreted as the effect of anisotropic hydrodynamic drag induced by the polymer–polymer interactions.
- The family of the *FENE* (Finitely Extensible Nonlinear Elastic) models are based on the kinetic theory of polymer chains behaving like non-linear elastic springs and are adapted to represent the viscoelastic behavior of dilute polymeric solutions.

It is well known that most viscoelastic computations based on the conformation tensor encounters numerical instabilities at some limiting value of the Weissenberg number. This problem know as *High Weissenberg Number Problem (HWNP)* is due the extension of large stresses, and stress gradients in narrow regions of the flow domain. This problem remains the main difficulty in numerical simulation of viscoelastic fluid flow. HWNP happens independent of the selected discretization technique, i.e. finite-difference, finite-volume or finite-element methods all have encountered this problem. In order to handle HWNP in numerical simulations of viscoelastic fluids, several stabilization approaches have been promoted. Although none of these approaches completely solves the problem, they enable us to stably simulate the viscoelastic flow at Weissenberg numbers close to the applications. The most outstanding approaches in the field of finite-volume are *both-sides diffusion* (BSD), the *positive definiteness preserving scheme* (PDPS) by Stewart et al. [61], the *log-conformation tensor representation* (LCR) by Fattal and Kupferman [62] and the *square-root-conformation representation* (SRCR) by Balci et al. [63]. Each of these approaches has their advantages and disadvantage and knowing them beforehand is important in choosing the appropriate approaches to cope with different kinds of stability problems caused by large Weissenberg number or by small viscosity ratios as well as to fulfill different requirements such as high accuracy, low computation cost etc.

According to Amoreira and Oliveira [64], the absence of an explicit diffusive term in the momentum equation including viscoelastic constitutive equation causes numerical instabilities in the convergence of iterative algorithms. A common practice to deal with this instability is to include extra diffusive terms on both sides of the momentum equation in which one is treated explicitly like a source and the other one implicitly. According to Sarkar and Schowalter [65], in this method which is called BSD, this implicit term gives rise to the algebraic coefficients that regulate convergence of the iterative numerical algorithm

Three other mentioned approaches of PDPS, LCR and SRCR are based on the positive definiteness preserving of the conformation tensor. Besides the LCR or SRCR, it is possible to obtain other logarithm-based, root-based or more generic transformations for the constitutive equation of the conformation tensor, aiming at resolving the exponential growth of the stress. For instance, Afonso, Pinho, and Alves [66] presented a general kernel-conformation tensor transformation for a large class of different constitutive models. Chen et al. [67] comprehensively analyzed the implementation and application of four approaches of BSD, PDPS, LCR and SRCR in stabilization of finite-volume viscoelastic fluids compared with standard discretization of constitutive equation. According to them:

- BSD and PDPS are more convenient to implement than LCR and SRCR. Comparing the last two approaches, SRCR could be implemented with less effort.
- Regarding the high Weissenberg number problem, LCR and SRCR are more stable compared to PDPS, BSC and standard formulation of the constitutive equation. Despite the BSD approach, PDPS preserves the positive definiteness of the conformation tensor. However, an attractive advantage of BSD is its ability to well resolve the instability problem caused by small viscosity ratios. Besides, because of its low implementation complexity, this approach could be coupled with other stabilisation approaches to deal with both numerical instability problems of HWNP and small viscosity ratios.

1.0.3 Non-Newtonian Fluid-Structure Interaction Problems

Many numerical methods have been developed to accurately simulate fluid-structure interaction problems. However, most of the previous works have studied the interaction of a Newtonian fluid with an elastic structure. Although Newtonian fluids account for many important problems, there are many practical situations where the working fluid cannot be modeled as Newtonian. Thus the mathematical modeling for simulation of the FSI problem must account for the non-Newtonian behavior of the fluid as well.

For example the Navier-Stokes equations of an incompressible viscous fluid are a good approximation for blood flow in medium-to-large arteries, such as the coronary arteries and the abdominal aorta. However, in order to solve the blood flow in the microcirculation, where the flow rates are low, the non-Newtonian rheological behaviour of blood including shear-thinning and viscoelastic cannot be ignored [68, 69]. The choice of the constitutive equation is of high importance in balancing the computational cost, thermodynamic consistency of the models, and microstructural insight.

Despite many numerical methods proposed for non-Newtonian fluids, few works in the literature have studied the problem of a non-Newtonian fluid interacting with a deforming structure. Also, In spite of significant progress in the field of single phase viscoelastic fluid flow, the key questions in the field of non-Newtonian Viscoelastic Fluid-Structure Interaction (VFSI) has not been answered and works in this area are limited in numbers. Chakraborty and Prakash [70] studied the flow in a 2D collapsible channel considering three different viscoelastic fluid models of the Oldroyd-B, the FENE-P and the Owens model [71] for blood. In their study, the collapsible channel consisted of a deformable wall of finite-thickness incompressible neo-Hookean solid. In their work, the channel dimensions are compatible with the microcirculation. Lukácova-Medvidova and Zaušková [72] investigated the numerical modelling of non-Newtonian flow in two-dimensional compliant vessels with application in hemodynamics for shear-thinnig fluids and compared the results with Newtonian fluids. Chen, Schäfer, and Bothe [73] used an implicit partitioned coupling algorithm to investigate the interaction between a viscoelastic Oldroyd-B fluid and an elastic structure for a flow through a channel with a flexible wall and a lid-driven cavity flow with flexible bottom. They reported that the solid deformation is influenced by the Weissenberg number in the fluid flow in both forced and free oscillation.

In this study we propose a numerical method to study the non-Newtonian shear-thinning/shear-thickening/viscoelastic fluid interacting with an elastic structure. We use a semi-implicit approach to develop an efficient coupling technique for non-Newtonian FSI problems with strong added-mass effect.

Chapter 2

Mathematical Formulations

In this chapter, the governing equations for each sub-problem domain and the coupling conditions on the interface are presented. The fluid and structural domains are referred to as $\Omega_f(t)$ and $\Omega_s(t)$ respectively, as they both vary in time. The interface of the domains is the shared boundary denoted by $\Gamma(t) = \partial\Omega_f(t) \cap \partial\Omega_s(t)$. An Arbitrary Lagrangian-Eulerian (ALE) formulation together with a conforming mesh technique is used to solve the fluid flow in a moving domain. A Lagrangian formulation is used for the structural equations.

2.0.1 Fluid equations

The unsteady flow of an incompressible fluid is governed by the Navier-Stokes equations. An Arbitrary Lagrangian-Eulerian (ALE) formulation of these equations in a moving domain is given by:

$$\frac{\partial \mathbf{u}}{\partial t} + \mathbf{c} \cdot \nabla \mathbf{u} = \frac{1}{\rho_f} \nabla \cdot \sigma_f \tag{2.1}$$

$$\nabla \cdot \mathbf{u} = 0 \tag{2.2}$$

where $\mathbf{u}$ is the fluid velocity and ρ_f the fluid density. Vector $\mathbf{c}$ is the ALE convective velocity $\mathbf{c} = \mathbf{u} - \mathbf{w}$, which is the fluid velocity relative to a domain moving with a velocity $\mathbf{w}$. The stress tensor σ_f is defined as:

$$\sigma_f = -p\mathbf{I} + 2\mu_s\dot{\gamma} + \mu_p\tau \tag{2.3}$$

where p is the fluid pressure, $\mathbf{I}$ the unit tensor, μ_s the dynamic viscosity of the solvent, μ_p is the dynamic viscosity of the polymeric part and $\dot{\gamma}$ the strain rate tensor given by:

$$\dot{\gamma} = \frac{1}{2}(\nabla\mathbf{u} + \nabla\mathbf{u}^T) \tag{2.4}$$

In equation 2.3, τ is the extra stress tensor related to non-Newtonian viscoelastic behaviour of the fluid. The Oldroyd-B constitutive equation is used to model this extra stress tensor as follow:

$$\tau + \lambda\overset{\nabla}{\tau} = 2\mu_p\dot{\gamma} \tag{2.5}$$

where λ is the relaxation time characteristic of viscoelastic fluid. In this formulation $\overset{\nabla}{\tau}$ is the upper convected time derivative of stress tensor. This operator for an arbitrary tensor of A defines as:

$$\overset{\nabla}{A} = \frac{\partial A}{\partial t} + u.\nabla A - \nabla u^T.A - A.\nabla u \tag{2.6}$$

2.0.2 Structural equations

The structural domain is governed by the nonlinear elastodynamics equation:

$$\rho_s\frac{D^2\mathbf{d}}{Dt^2} = \nabla\cdot\sigma_s \tag{2.7}$$

where $\mathbf{d}$ stands for the structural position with respect to the reference configuration, and the structural density is shown by ρ_s. The Cauchy stress tensor σ_s is related to the second Piola-Kirchhoff tensor $\mathbf{S}_s$ by:

$$\mathbf{S}_s = J\mathbf{F}^{-1}\sigma_s\mathbf{F}^T \tag{2.8}$$

where $\mathbf{F}$ is the deformation gradient $\mathbf{F} = \nabla\mathbf{d}$ and J is its determinant ($J = det(\mathbf{F})$).

The FSI method is presented for a general structure, however, for the test case in this paper the structure is considered to be an Euler-Bernoulli beam with stress applied from fluid added to it, governed by the following equation:

$$\rho A \frac{\partial^2 \mathbf{d}}{\partial t^2} + \frac{\partial^2}{\partial x^2}\left(EI \frac{\partial^2 \mathbf{d}}{\partial x^2} \right) = q(x,t) + \frac{h}{2} \frac{\partial g(x,t)}{\partial x} \tag{2.9}$$

where $\mathbf{d} = [0,y,0]^T$ in a Cartesian coordinate (x,y,z), A is the cross section area of the beam and I is the second moment of area. In this formulation, **q**(x,t) and **g**(x,t) are the normal and tangential force of per unit length components of stress tensor.

2.0.3 Coupling conditions

The coupling conditions apply at the interface Γ and account for the interaction of the domains. They are derived from the kinematic and dynamic equilibrium between the domains, which yield to the following conditions on a non-slip type interface:

$$\mathbf{u}_\Gamma = \frac{\partial \mathbf{d}_\Gamma}{\partial t} \tag{2.10}$$

$$\sigma_s \cdot \mathbf{n}_\Gamma = \sigma_f \cdot \mathbf{n}_\Gamma \tag{2.11}$$

for any point $\mathbf{x} \in \Gamma$, where $\mathbf{n}_\Gamma$ is the unit normal vector on the interface. Equation (2.10) represents equality of the velocity of the fluid and the structure on the interface to assure the kinematic equilibrium. Equation (2.11) represents equality of the traction on the interface for dynamic equilibrium.

2.1 Numerical Method

In this section we represent the numerical methods and discretization schemes to solve the coupled non-linear system of governing equations.

2.1.1 Fluid solver

A fractional-step (projection) method [74] is used to solve the velocity/pressure coupling of the momentum equation. Thus, an intermediate velocity field is evaluated without considering the pressure gradient term. We use an explicit Adams-Bashforth method for discretization of the convective and diffusive terms. Therefore the intermediate velocity field is evaluated as:

$$\frac{\rho_f \mathbf{u}^* - \rho_f \mathbf{u}^n}{\Delta t} = \frac{3}{2}(R_h^u)^n - \frac{1}{2}(R_h^u)^{n-1} \tag{2.12}$$

where $R_h^u = -\mathbf{C}_h(\rho_f \mathbf{u}) + \mathbf{D}_h(\mathbf{u})$ with $\mathbf{C}_h(\rho_f \mathbf{u}) = \nabla_h \cdot (\rho_f \mathbf{u}\mathbf{u})$ as the convective operator and $\mathbf{D}_h(\mathbf{u}) = \nabla_h \cdot (2\mu_s \dot{\gamma} + \mu_p \tau)$ as the diffusive operator for any $\mathbf{x} \in \Omega_f^{n+1}$. This velocity field is then projected onto a space of divergence-free vector fields:

$$\mathbf{u}^* = \mathbf{u}^{n+1} + \frac{\Delta t}{\rho_f} \nabla p^{n+1} \tag{2.13}$$

$$\nabla \cdot \mathbf{u}^{n+1} = 0 \tag{2.14}$$

where p^{n+1} is the pressure field obtained by:

$$\nabla p^{n+1} = \frac{\rho_f}{\Delta t} \nabla \cdot \mathbf{u}^* \tag{2.15}$$

A conjugate gradient solver with a diagonal pre-conditioner is used to solve the Poisson's equation.

The boundary condition for velocity on the interface comes from the coupling condition:

$$\mathbf{u}_\Gamma^{n+1} = \frac{\mathbf{d}_\Gamma^{n+1} - \mathbf{d}_\Gamma^n}{\Delta t} \tag{2.16}$$

for any $\mathbf{x} \in \Gamma^{n+1}$. We apply this boundary condition on the predicted velocity as well:

$$\mathbf{u}_\Gamma^* = \frac{\mathbf{d}_\Gamma^{n+1} - \mathbf{d}_\Gamma^n}{\Delta t} \tag{2.17}$$

In this work, the fractional-step method is used not only for solving the fluid equations, but also as a framework for the overall FSI solution algorithm, making it fundamental to the overall method.

2.1.2 Dynamic mesh

As the solid boundary is deformable, fluid mesh needs to move to adapt to the new location of the interface and the discrete domain velocity on the mesh surfaces $\mathbf{w}^{n+1}$ needs to be evaluated. A parallel moving mesh technique, based on radial basis function interpolation method [75], is used to move the fluid grid in accordance to the new location of the interface. Surface velocities are evaluated according to the so-called space conservation law which guarantees no volume is lost while moving the grid. Detailed description of the dynamic mesh method could be found in [75, 11, 76]. Figure 2.1 schematically compares the original discretized domain with a deformed discretized domain for a test case of lid-driven cavity with elastic wall at the bottom using described dynamic mesh algorithm. Here we will use the function $\mathscr{M}$ to refer to the mesh movement step:

$$(\Omega_f^{n+1}, \mathbf{w}^{n+1}) = \mathscr{M}(\mathbf{d}_\Gamma^{n+1}) \tag{2.18}$$

2.1.3 Structural solver

Structural equations are discretized in time using a second-order Newmark method. Defining the structural velocity $\mathbf{v} = \frac{\partial \mathbf{d}}{\partial t}$, the semi-discretized structural equation reads:

$$\mathbf{v}^{n+1} = \mathbf{v}^n + \frac{\Delta t}{2\rho_s A}[(q^{n+1} - EI\frac{\partial^4 \mathbf{d}}{\partial x^4})^{n+1} + (q^n - EI\frac{\partial^4 \mathbf{d}}{\partial x^4})^n] \tag{2.19}$$

and the new location of the structure could be calculated as:

$$\mathbf{d}^{n+1} = \mathbf{d}^n + \frac{\Delta t}{2}(\mathbf{v}^{n+1} + \mathbf{v}^n) \tag{2.20}$$

It should be noted that using a simplified structural model is not restrictive for the proposed FSI coupling method, since it is used as a black-box module. We will use the notation $\mathscr{S}$ to refer to the structural solver as a function of surface stress on the interface:

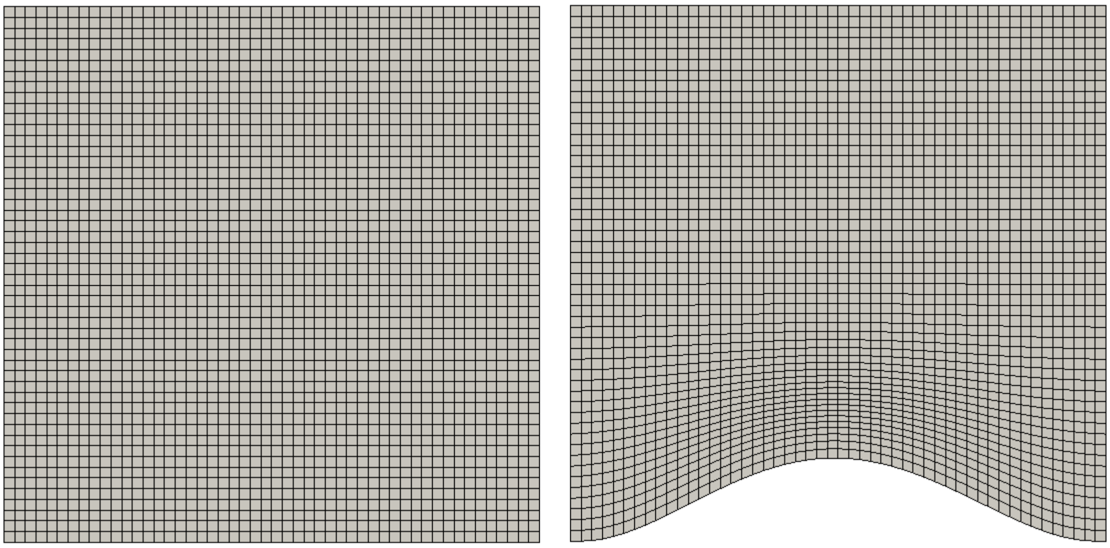

FIGURE 2.1: Comparison between (left) the original discretized domain and (right) a deformed discretized domain for a test case of lid-driven cavity with elastic wall at the bottom.

$$\mathbf{d}_\Gamma = \mathscr{S}(\sigma_\Gamma) \tag{2.21}$$

where $\mathbf{d}_\Gamma$ is the location of the interface and σ_Γ is the stress on the interface exerted by the fluid $\sigma_\Gamma = \sigma_f(p, \mathbf{u})_\Gamma \cdot \mathbf{n}_\Gamma$.

2.1.4 Coupling method

A semi-implicit FSI coupling method developed by Naseri et al. [27], is used in which only the fluid pressure term is strongly coupled to the structure via coupling iterations. The remaining fluid terms as well as the dynamic mesh step are evaluated only once per time step.

The FSI solution method at a new time step is as follows.

step 1- Explicit step:

- Predict the location of the interface by extrapolation from previous time steps.
- Define the new discretized domain using equation 2.18.

- Evaluate the predicted velocity field by equation **??**.

step 2- Implicit step:

- Evaluate the fluid pressure (equation 2.15)
- Solve the structural equations to evaluate the deformation (equation 2.21).
- Update the boundary condition on predicted velocity (equation 2.17).
- Repeat until convergence is achieved.

step 3- Explicit step:

- Correct the velocity field (equation 2.13)
- Apply the boundary condition for velocity (equation 2.16).

Step 2 of the above algorithm is where fluid pressure is strongly coupled to the structure. This step provides for the stability of the method for FSI problems with strong added-mass effect.

Chapter 3

Numerical Experiments and Discussion

In this chapter, the results regarding the flow in classical lid-driven cavity test case will be presented. The lid-driven cavity problem has long been used a test or validation case for new codes or new solution methods. This problem is of particular interest for testing for several reasons. There are many data available extracted from different experimental studies and numerical methods. The laminar solution of the flow is steady. Plus, the problem's geometry is simple and two-dimensional, boundary conditions are simple and easy to implement.

Numerical tests of this section are carried out on a benchmark problem studied in [22, 16], among others. The test case is a 2-D lid-driven cavity of $L \times L$ with a flexible bottom. The top boundary of the cavity is moving with a velocity of u(x,t). There are two openings of $0.1L$ on the sidewalls that allow the fluid to enter to and exit from the domain. Figure 3.1 shows a schematic description of the problem.

Dimensionless parameters of Reynolds number, Weissenberg number, retardation ratio and c_λ are defined to non-dimensionalize the problem. Reynolds number is the ratio of inertial forces to viscous forces in the fluid, Weissenberg number compares the elastic forces to the viscous forces of viscoelastic fluid, retardation ratio β (or solvent viscosity ratio) is the ratio of solvent viscosity of viscoelastic fluid to its total viscosity, and c_λ describes the extensional stiffness of the structure. These parameters are defined as :

$$Re = \frac{\rho_f U L}{\mu_0}, \quad Wi = \frac{\lambda_1 U}{L}, \quad \beta = \frac{\lambda_2}{\lambda_1}, \quad c_\lambda = \frac{Eh}{\rho_f U^2 L} \tag{3.1}$$

where U and L are characteristic velocity and length of the cavity, respectively. λ_1 is

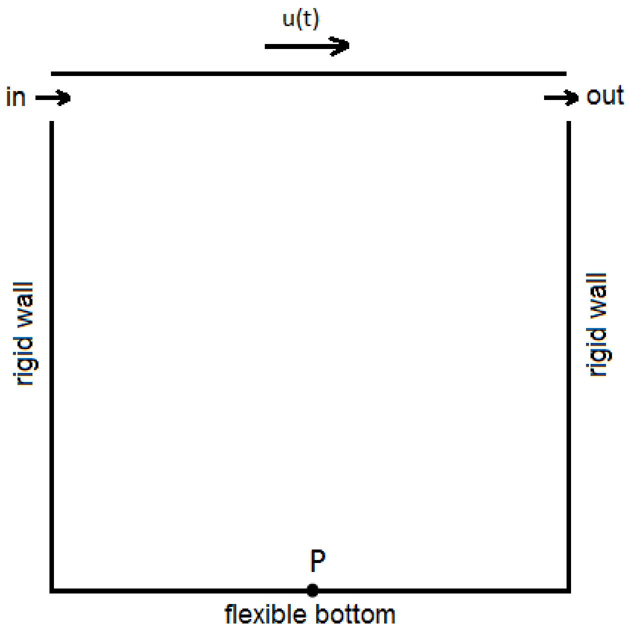

FIGURE 3.1: Schematic view of the driven cavity test case with flexible bottom wall. Point P is the midpoint of bottom wall.

relaxation time of the viscoelastic fluid, ρ_f is the fluid viscosity, μ_0 is the total viscosity of the fluid, E is the structural Young modulus, and h is the thickness of flexible structure at the bottom. In all the simulations, time is being non-dimensionalized as $t' = t/t^*$ with $t^* = L/U$.

Two different mesh types of structured and unstructured with the grid size of ℓ= $0.01L$ (with ℓ as the edge size of the grid) are used to discretize the domain. Spatial discretization is carried out using a finite volume method with second-order central difference schemes for diffusive terms and upwind scheme for convective terms. Figure 3.2 illustrates the discretized domain used in this section. The structure is a thin membrane so the fluid mesh elements on the interface are also used as the computational grid for the structural equations. Thus, the structural grid nodes match the fluid mesh on the interface and there is no need for interpolation of parameters between the domains.

Firstly, in order to make sure of the accuracy of the viscoelastic solver, the structural solver is being turned off. Then we study the numerical solution of an Oldroyd-B flow inside of the lid-driven cavity using proposed method. The results are compared with the

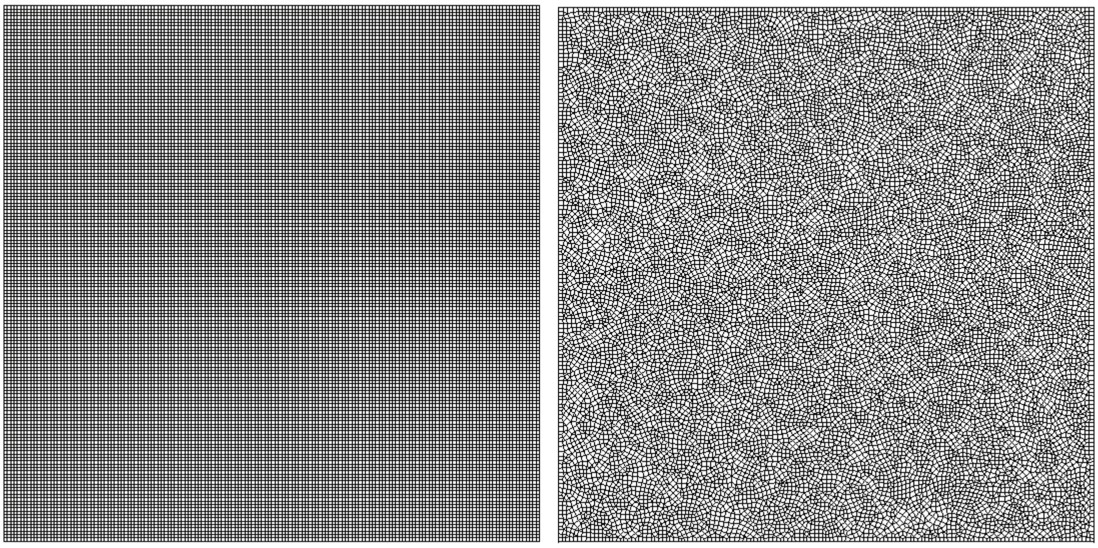

FIGURE 3.2: Two different mesh types of structured and unstructured used in discretization of lid-driven cavity problem.

results of Yapici, Karasozen, and Uludag [77]. To eliminate the singularities at the corners, the top wall moves with the space and time-dependent velocity profile as below:

$$u(x,t) = 8[1 + tanh(8t-4)]x^2(1-x^2) \tag{3.2}$$

The lid velocity gradually increases until it reaches its maximum magnitude at the center of the lid. The simulation runs long enough until the flow reaches its steady-state. No-slip boundary condition is fixed on all other walls. Simulation with Re=100, Wi=0.7 and β=0.3 are done in domains with two different mesh types of Structured and Unstructured. The u(y) and v(x) velocity profiles at the mid-plane normal to x and y directions are extracted for these simulations. These results are shown in figure 3.3 and are compared with the finite-volume results of Yapici, Karasozen, and Uludag [77]. According to this figure, very good agreement is seen between the results of this study for fixed mesh with structural interaction excluded and the benchmark result. It is noteworthy that the results in structured and unstructured meshes are almost identical.

As the next step, now that we are assure of the good accuracy of viscoelastic fluid solver, and keeping in mind that the structural solver has been already validated against

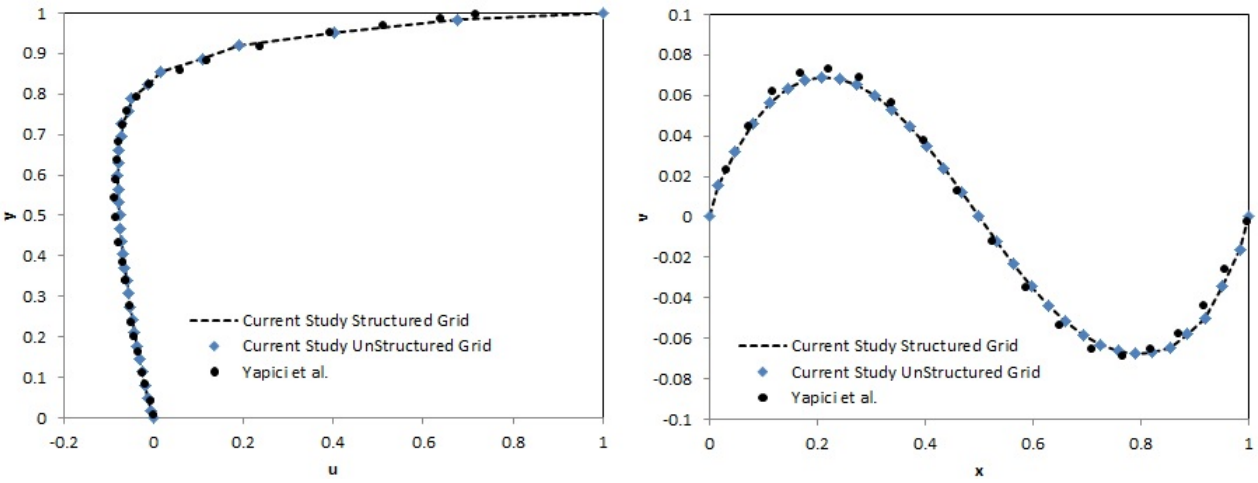

FIGURE 3.3: Left: u(y) and right: v(x) velocity profiles at the mid-plane normal to x and y directions, of lid-driven cavity test case for a viscoelastic fluid with Re=100, Wi=0.7 and $\beta = 0.3$ in a fixed mesh geometry (structural interactions excluded) compared with the reference data of Yapici, Karasozen, and Uludag [77].

experimental data, we perform simulation in which the top wall is oscillating with a speed of:

$$u(x,t) = 16\,(1 - cos(\omega t))\,x^2(1-x)^2 \tag{3.3}$$

with $\omega = 2\pi/5$. In this formulation of velocity, the lid oscillates in time with a constant frequency, and as well is varying in x direction, in order to avoid singularities at the corners in case of viscoelastic fluids. Figure 3.4 illustrates the value of u(x,t) for this case for different x and t values.

In the simulations of fluid-structure interactions, the value of c_λ is chosen to be equal to 12.5 and two parameters of ρ_s/ρ_f and **h**/L are 20 and 0.05, respectively. Simulations are carried out from $t' = 0$ until $t' = 30$. The list of simulations performed with different rheological properties are tabulated in table 3.1. For the cases with shear-thinning fluids, Generalized Newtonian Fluid model of power-law as described in equation 1.2 with different **n** indices is used. For the case of viscoelastic fluids, and Oldroyd-B constitutive equation as discussed in section 1.0.2 with different values of Weissenberg numbers and retardation ratios is being used. For the cases of $Wi = 0.75$ and $Wi = 1.0$, the standard

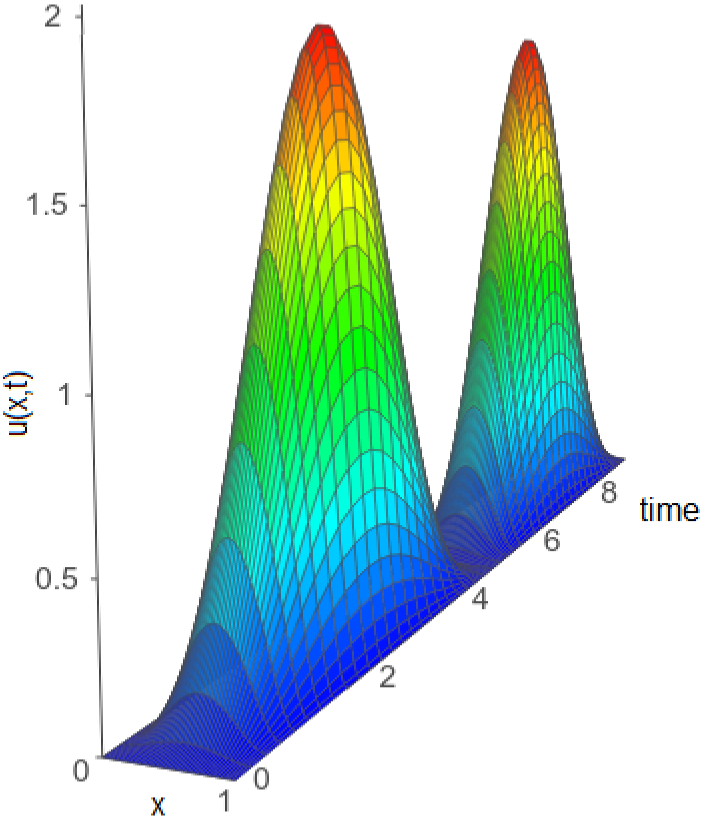

FIGURE 3.4: An schematic illustration of u(x,t) function in time and space used in test cases with flexible bottom.

formulation of constitutive equation results in numerical difficulties regarding the convergence of simulations. In order to deal with this issue, for these cases, the log-conformation representation of constitutive equation is being used to solve the problem. For the case with shear-thickening fluid, the piecewise function of equation 1.5 is used to describe the variation of apparent viscosity by shear-rates. The value of μ_0 in this case is obtained from Reynolds number of the flow which is equal to 100. The value of other parameters of shear-thickening test case are chosen in a way so that the shear-rate is more or less in the same order of magnitude of its corresponding Newtonian fluid enabling us to witness the three

TABLE 3.1: Summary of numerical simulations carried out in order to study fluids with different rheological properties interacting with elastic structure in the content of lid-driven cavity test case.

Name	Fluid's rheology	Properties	Formulation
NFSI	Newtonian	-	-
$VFSI_1$	Viscoelastic	**Wi**=0.25, $\beta = 0.3$	Oldroyd_B-SVF
$VFSI_2$	Viscoelastic	**Wi**=0.50, $\beta = 0.3$	Oldroyd_B-SVF
$VFSI_3$	Viscoelastic	**Wi**=0.75, $\beta = 0.3$	Oldroyd_B-LCR
$VFSI_4$	Viscoelastic	**Wi**=1.00, $\beta = 0.3$	Oldroyd_B-LCR
$VFSI_5$	Viscoelastic	**Wi**=0.25, $\beta = 0.6$	Oldroyd_B-SVF
$VFSI_6$	Viscoelastic	**Wi**=0.50, $\beta = 0.6$	Oldroyd_B-SVF
$VFSI_7$	Viscoelastic	**Wi**=0.75, $\beta = 0.6$	Oldroyd_B-LCR
$VFSI_8$	Viscoelastic	**Wi**=1.00, $\beta = 0.6$	Oldroyd_B-LCR
$SThinningF_1$	Shear-Thinning	**n**=0.75	Power-Law
$SThinningF_2$	Shear-Thinning	**n**=0.50	Power-Law
STF_1	Shear-Thickening	Eq. 3.4	Piecewise function of [48]

regions of STFs as described in figure 1.4. These parameters are as below:

$$(\mu_0, \lambda_I, n_1, \mu_c, \dot{\gamma}_c, \lambda_{II}, n_{II}, \mu_{max}, \dot{\gamma}_{max}, \lambda_{III}, n_3) = (0.01, 5000, 0.9, 0.005, 0.007, 142.8, 1.05, 0.035, 0.5, 0.2, 0.8) \quad (3.4)$$

Figure 3.5 represents the viscosity curve of the shear-thickening fluid used in the test case of STF_1, with parameters defined in 3.4. The comparisons of the results regarding different cases are done in two aspects. One is related to the flow inside of the domain, and other is related to the structure response and deformation. For the first one, the u(y) and v(x) velocity profiles at the mid-plane normal to x and y directions, along with the flow streamlines, velocity and pressure contours in the domain are extracted. For the second one, time dependent oscillation of point P (as shown in 3.1) in y direction is extracted.

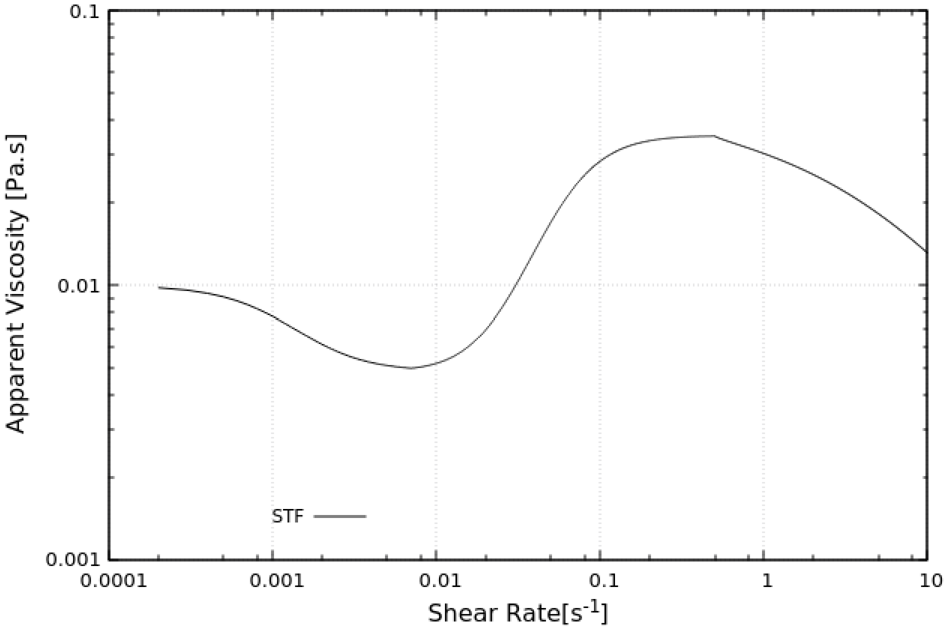

FIGURE 3.5: Viscosity curves of the shear-thickenning fluid used in test case of STF

First we analyze the effect of different rheologies of Newtonian, viscoelastic, shear-thickening and shear-thinning on fluid's flow inside of the domain, as the first aspect of the comparison. Figure 3.6 represents the u(y) and v(x) velocity profiles for cases $VFSI_1$, $SThinningF_1$ and STF_1 compared with the Newtonian case of NFSI. In this figure, results regarding four different rheological properties are demonstrated in order to gain a general understanding of the effect of fluid's rheology on the velocity components in the domain. According to this figure, the magnitude of velocity components (both u and v) in the case of shear-thickening fluid is smaller that other cases. The **v** velocity component in the x-wise center-line of the domain is maximum for Newtonian fluid. The variation of **u** velocity component in the y-wise center-line of the domain for Newtonian fluid is totally different from other rheologies. These changes are a direct result of different rheological properties of fluid and its related structural response.

Figure 3.7 presents the pressure contours at $t' = 9$ for simulations of cases (a) NFSI, (b) $VFSI_1$, (c) STF_1 and (d) $SThinningF_1$ as described in table 3.1. According to this figure, the

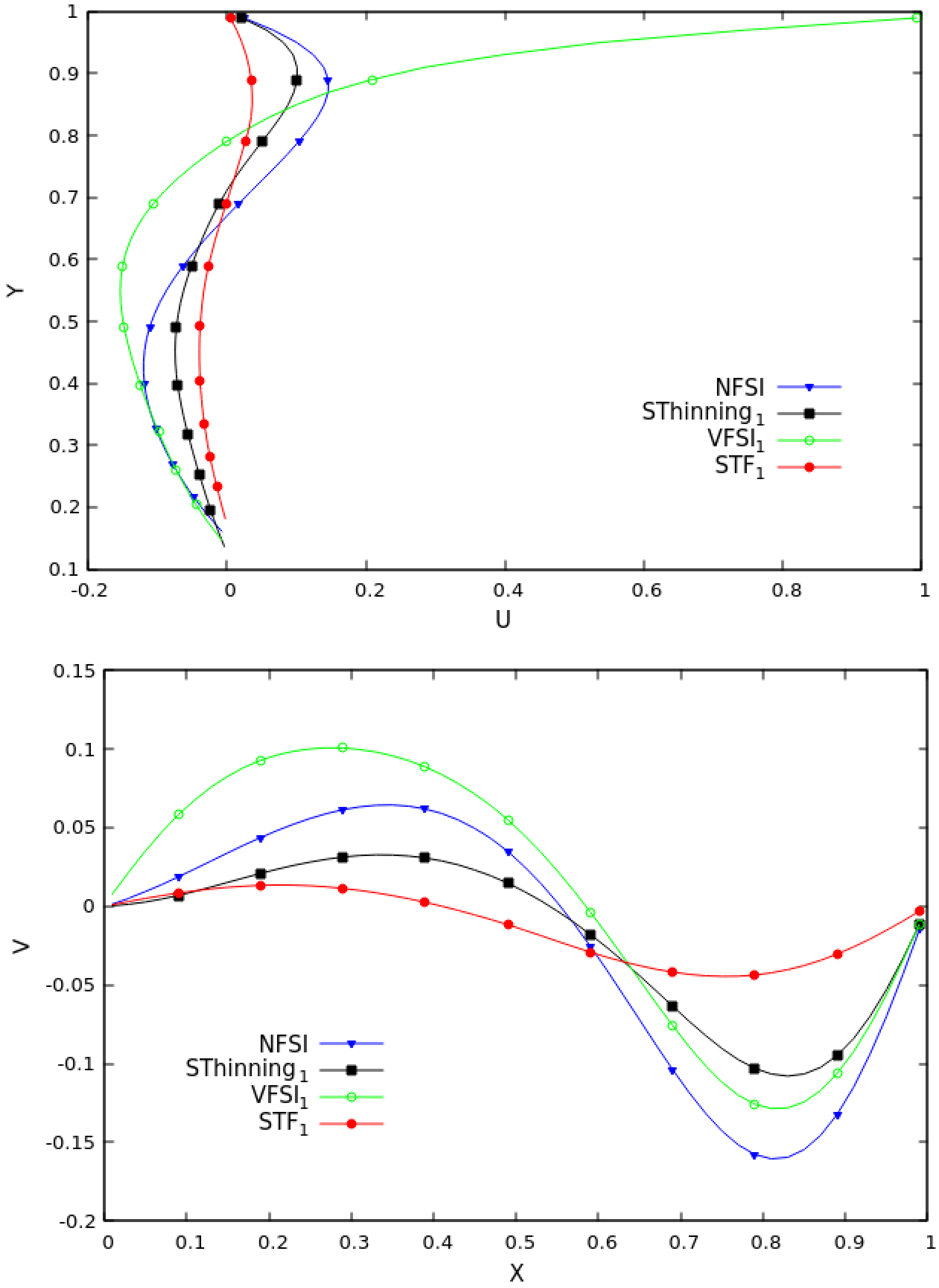

FIGURE 3.6: Top: u(y) and bottom: v(x) velocity profiles at the mid-plane normal to x and y directions, respectively, for different test cases of NFSI, $VFSI_1$, $SThinningF_1$ and STF_1 as described in table 3.1.

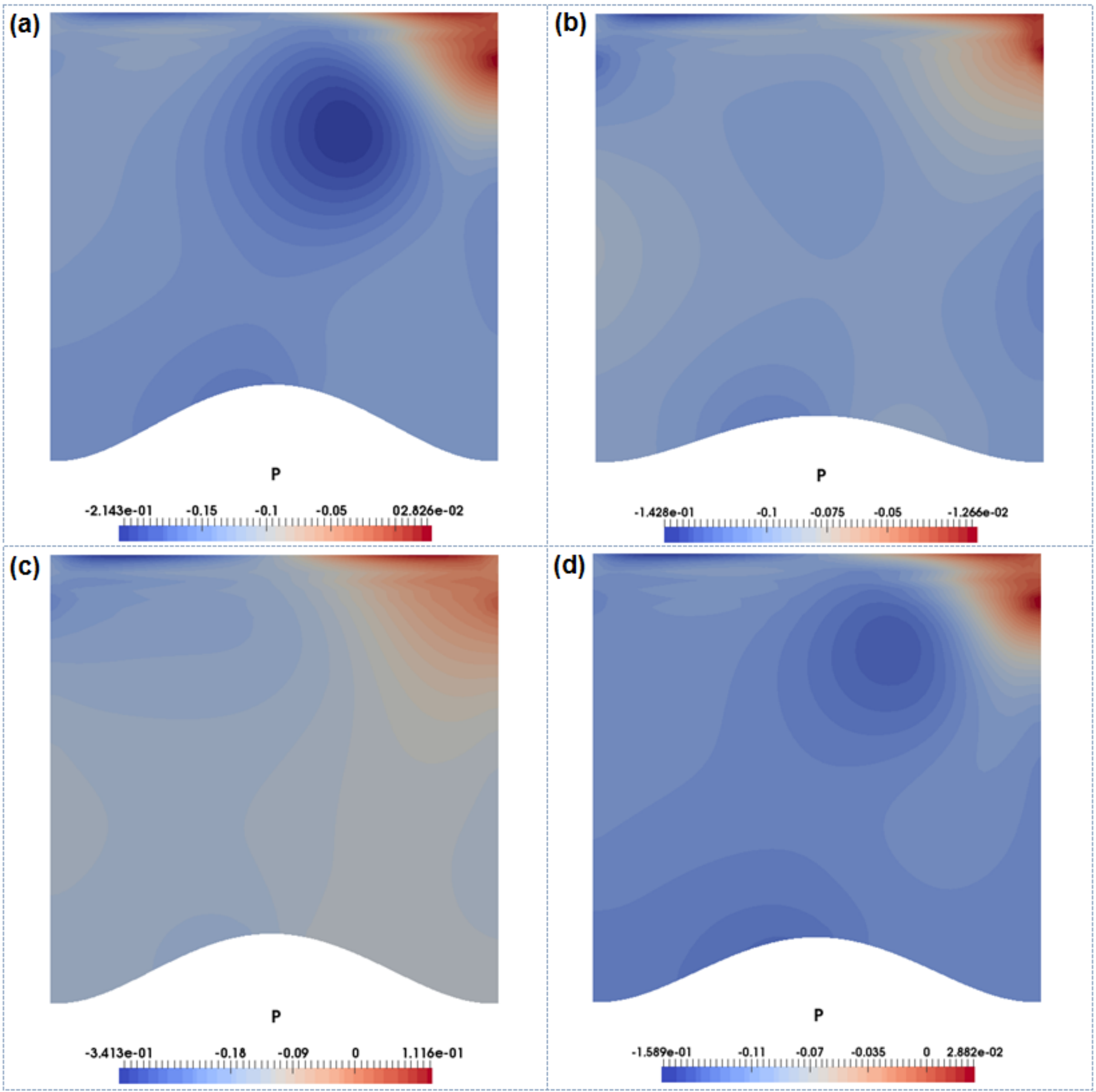

FIGURE 3.7: Pressure contours at $t' = 9$ for simulations of cases (a) NFSI, (b) $VFSI_1$, (c) STF_1 and (d) $SThinningF_1$ as described in table 3.1.

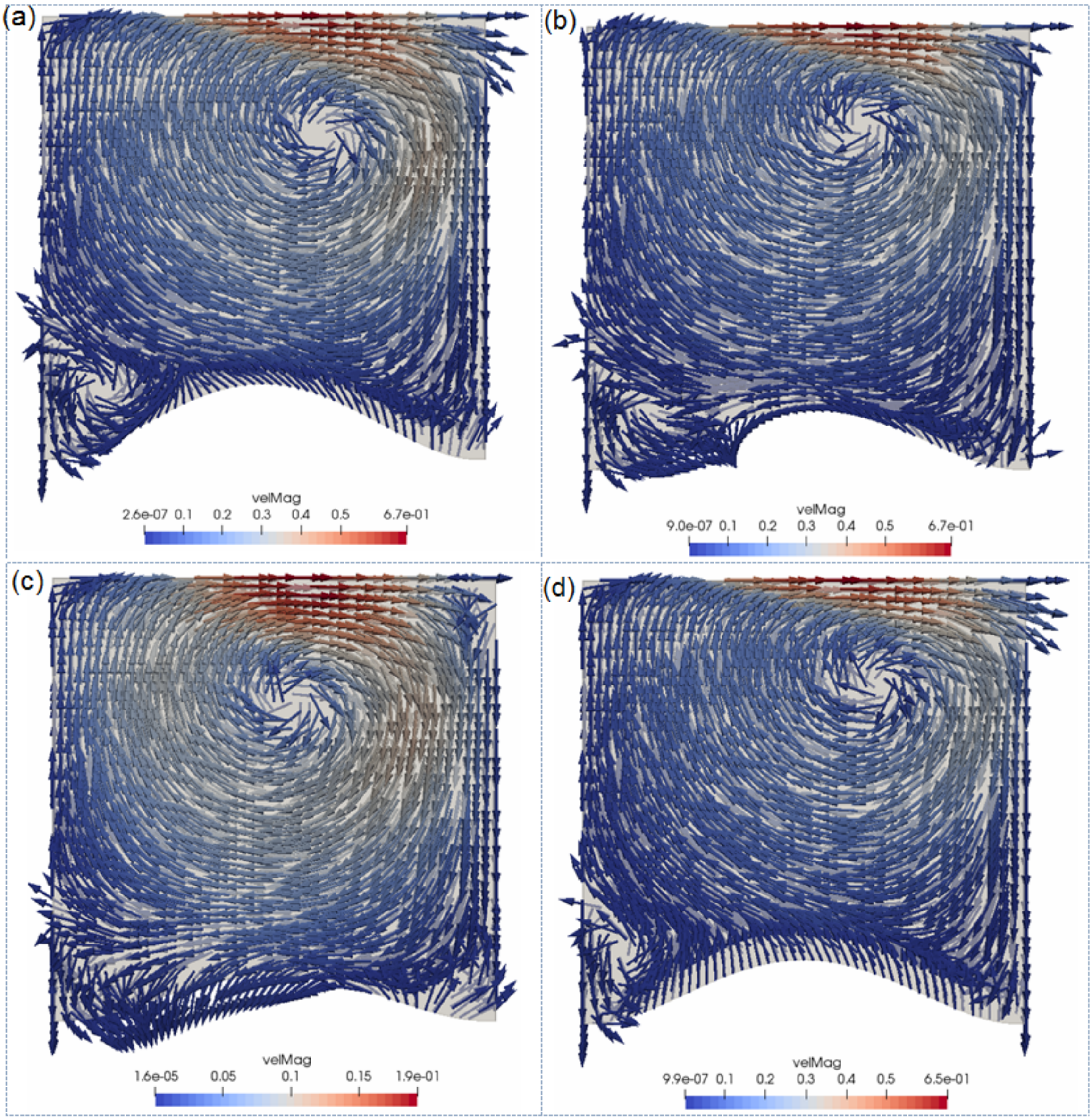

FIGURE 3.8: Velocity vectors of the fluid inside of the domain along with velocity magnitude contours at $t' = 9$ for simulations of cases (a) NFSI, (b) $VFSI_1$, (c) STF_1 and (d) $SThinningF_1$ as described in table 3.1.

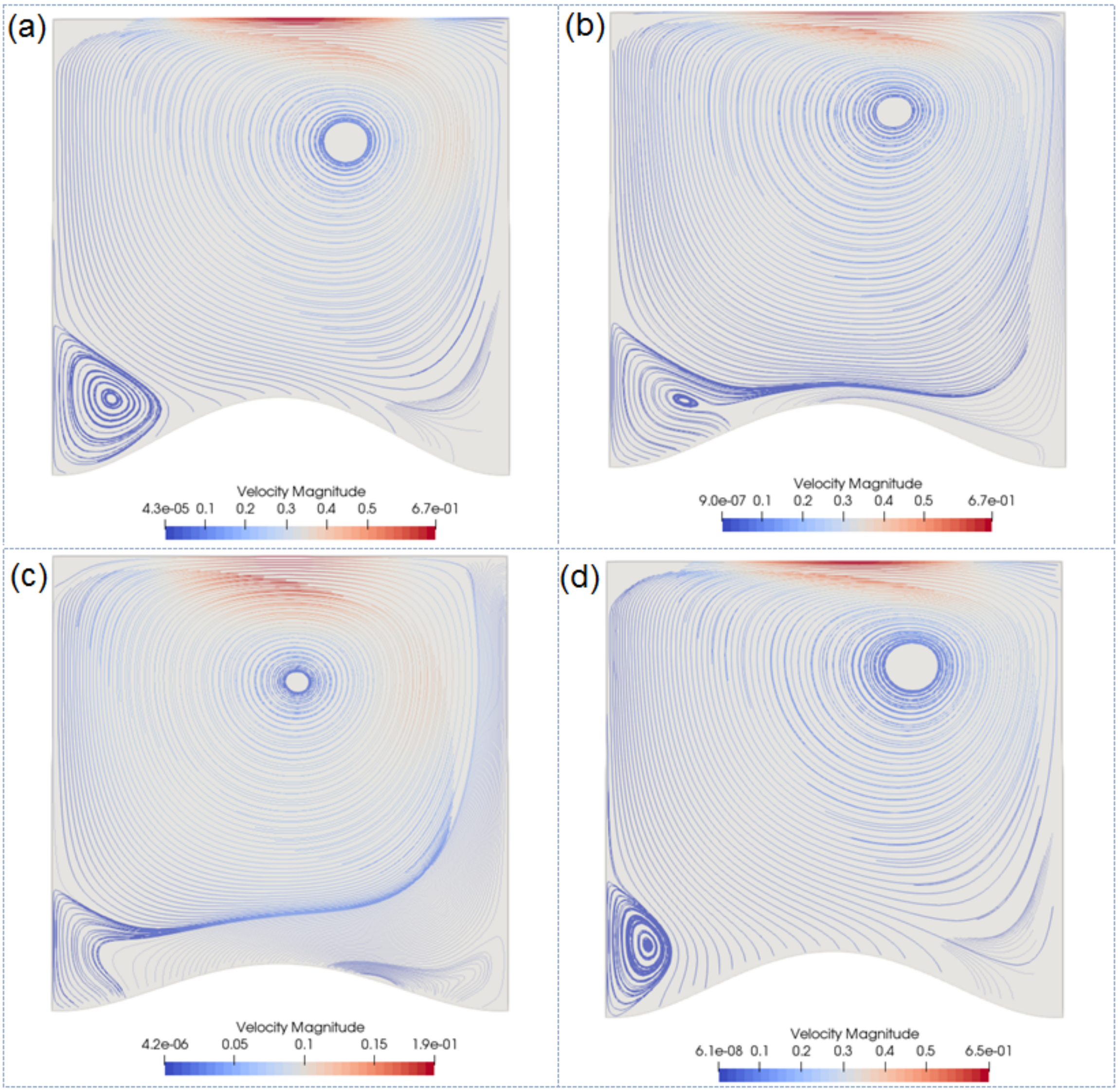

FIGURE 3.9: Streamlines of the fluid inside of the domain along with velocity magnitude contours at $t' = 9$ for simulations of cases (a) NFSI, (b) $VFSI_1$, (c) STF_1 and (d) $SThinningF_1$ as described in table 3.1.

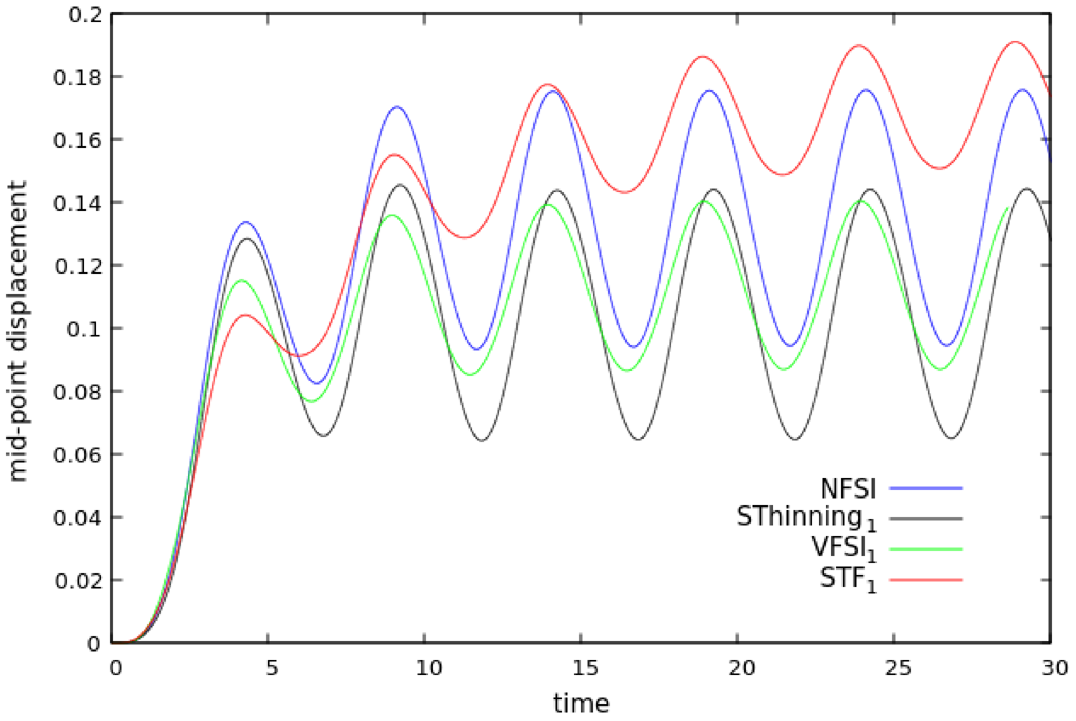

FIGURE 3.10: Displacement of point P as a function of time for different cases of NFSI, $VFSI_1$, $SThinningF_1$ and STF_1 as described in table 3.1.

pressure contours of cases NFSI and $SThinningF_1$ are similar to each other. On the other hands, the pressure contours of two cases of $VFSI_1$, and STF_1 are different from each other and also are different from the other two cases. In order to gain a better understanding on the flow behaviour inside of the domain, figure 3.8 illustrates the velocity vector representation of the flow inside of the domain and figure 3.9 illustrates the streamlines of the flow, both along with the velocity magnitude contours at $t' = 9$ for simulations of the same cases as figure 3.7. As can be seen in these figures, The main difference is in the flow around the left-bottom corner of the domain, where the biggest corner-vortex of Newtonian fluid in Re=100 forms. Changing the rheology of the fluid from Newtonian to shear-thickening fluid eliminates the vortex in the left-bottom of the domain and creates a somewhat different flow pattern in this region compare with other cases. In other cases of $VFSI_1$ and $SThinningF_1$, similar to the Newtonian fluid, there exists a vortex in the left-bottom corner

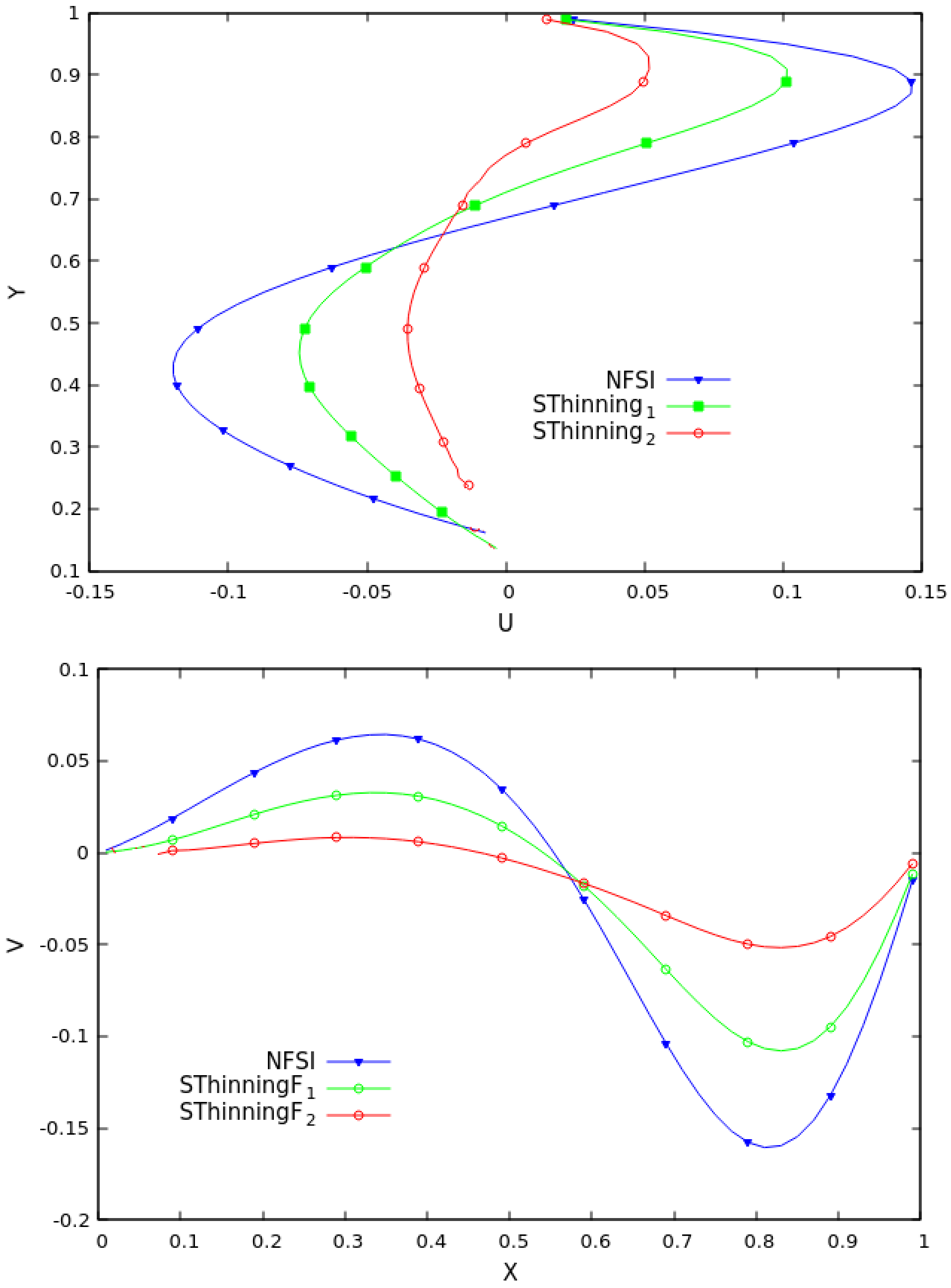

FIGURE 3.11: Top: u(y) and bottom: v(x) velocity profiles at the mid-plane normal to x and y directions, of lid-driven cavity test case for different test cases of NFSI, $SThinningF_1$ and $SThinningF_2$ as described in table 3.1.

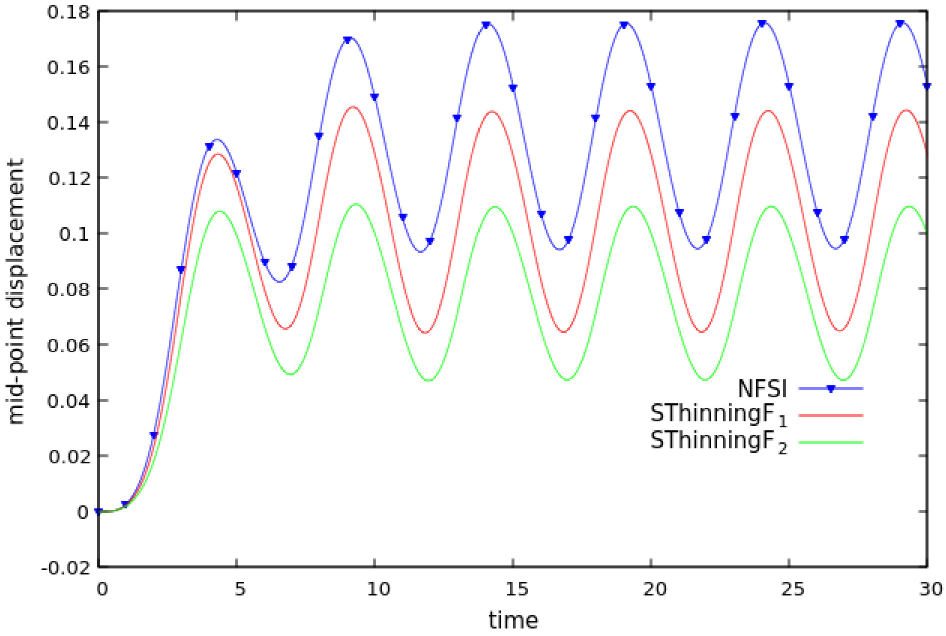

FIGURE 3.12: Displacement of point P as a function of time for different cases of NFSI, $SThinningF_1$ and $SThinningF_2$ as described in table 3.1.

of domain, however with different structure. The magnitude of the velocity inside of the domain for the cases of STF_1 is much smaller than other cases. This difference could be related to the shear-thickening nature of the fluid in this case. Keeping in mind that viscosity of a fluid is being defined as the measure of its resistance to gradual deformation by shear stress, since in the case of shear-thickening fluid the apparent viscosity of the fluid may increase due to the specific range of shear-rate, its resistance towards gradual deformation increases and as a result the velocity magnitude inside of the domain decreases.

In order to compare the structural response to different fluid rheologies, figure 3.10 demonstrates the displacement of point P as a function of time for different cases of NFSI, $VFSI_1$, $SThinningF_1$ and STF_1 of table 3.1. As can be seen in this figure, the minimum value of the deformations in oscillations regarding the case $SThinningF_1$ is lower compared with other cases. The peaks in deformation of cases $VFSI_1$ and STF_1 are slightly delayed compared with the shear-thinning and Newtonian fluids. The oscillations of point P in case of shear-thickening fluid (STF_1) is increasing by time and has not reached monotonous

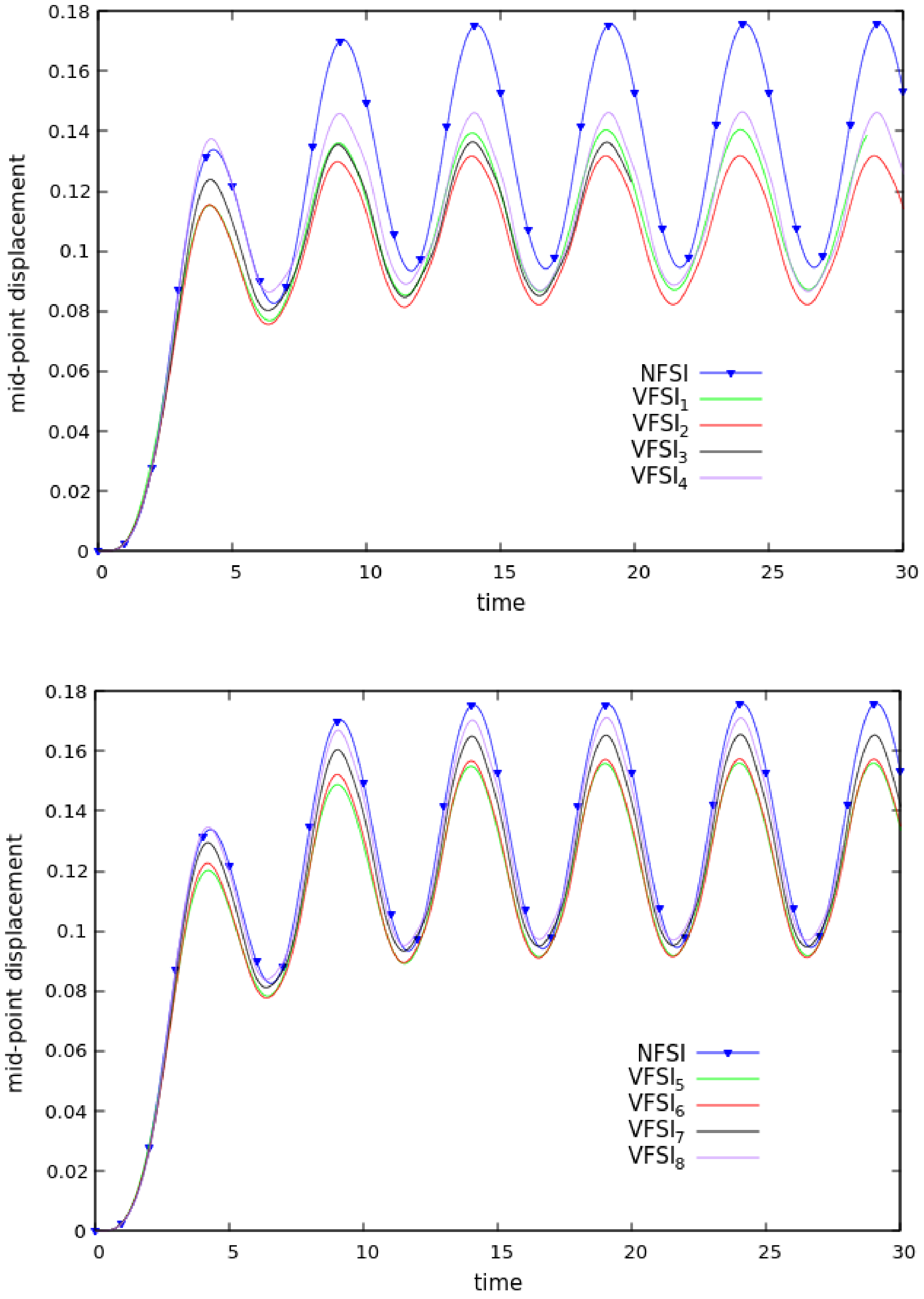

FIGURE 3.13: Displacement of point P as a function of time for cases, Top: $VFSI_1 : VFSI_4$ and Bottom: $VFSI_5 : VFSI_8$ compared with the case NFSI, as described in table 3.1.

variations within the timeframe of $t' = 30$ of the current study.

Now that some light has been shed on the effect of different rheologies of fluid inside a cavity with deformable bottom, more analyzing on the effect of power-law index **n** of shear-thinning fluids and Weissenberg number and retardation ratio of viscoelastic fluid on the acquired results, will be provided.

Figure 3.11 represents the u(y) and v(x) velocity profiles for cases $SThinningF_1$ and $SThinningF_2$, compared with the Newtonian case of NFSI. According to this figure, the magnitude of velocity components (both u and v) in the case of shear-thinning fluid is highly dependent on power-law factor, i.e. the strength of the shear-rate on changing the apparent viscosity. Figure 3.12 demonstrates the displacement of point P as a function of time for different cases of NFSI, $SThinningF_1$, and $SThinningF_2$ as described in table 3.1. It is clear to see that the magnitude of oscillations in both cases of shear-thinning fluids is smaller than the Newtonian fluid. By decreasing the power-law factor, i.e. increasing the effect of shear-thinning fluid, the value of oscillations of point P decreases.

Figure 3.13 presents the displacement of point P as a function of time for cases $VFSI_1$: $VFSI_8$ as described in table 3.1 in two categories of top figure, all cases with $\beta = 0.3$ and bottom figure, all cases with $\beta = 0.6$. This figure provides information regarding the effect of Weissenberg number and retardation ratio on dynamic response of the system over time compared with Newtonian fluid. According to this figure, the maximum deformation in structure decreases as fluid is being changed from Newtonian to viscoelastic. By increasing the Weissenberg number, the dynamic response of the system is getting more similar to the Newtonian fluid. This effect is more visible, specially for cases with higher β ($\beta = 0.6$). It can be seen that the deformation of elastic solid for Newtonian fluid is uniform and homogeneous in time, however, for viscoelastic fluid cases with smaller retardation ratio ($\beta = 0.3$), this variation is non-uniform specially after the maximum and minimum of deformations. For viscoelastic cases with higher retardation ratio ($\beta = 0.6$), the dynamic response of the system is uniform and homogeneous, similar to Newtonian Fluid. By increasing the Weissenberg number, the first peak of the deformation for times around $t' = 4$ for cases with small retardation ratio is as big as the rest of the peaks, which is different from other cases.

Chapter 4

Conclusion

A Numerical method for simulation of non-Newtonian (viscoelastic, shear-thinning and shear-thickening) fluid-structure interaction problems is presented. Oldroyd-B model is used as the constitutive equation for Viscoelastic fluid, power-law Generalized Newtonian Fluid model is used for shear-thinning fluids and a recently introduced piecewise function in the content of Generalized Newtonian Fluid is used to model shear-thickening fluids. A semi-implicit partitioned method is used to perform coupling between fluid and structure. Different cases of Newtonian/shear-thinning/shear-thickening/viscoelastic fluids with various rheological properties are tested for fluids inside a lid-driven cavity test case. The results show different flow patterns inside of the domain for different rheological properties of the fluid. For the case with shear-thickening fluid, the left-bottom corner vortex of cavity problem at Re=100 disappears. Dynamics response of the elastic wall to different rheological properties of the fluid is provided as well. According to the results provided, the deformation of the elastic wall could become non-uniform, as the fluid is being substituted by a viscoelastic fluid. According to the simulations performed, by increasing the retardation ratio of the viscoelastic fluid, the structural response of the elastic wall becomes more similar to the Newtonian fluid.

Numerical tests demonstrate the capability of the method to solve non-Newtonian FSI problems with a wide range of application in different areas.

Bibliography

[1] Andrew T Barker and Xiao-Chuan Cai. “Scalable parallel methods for monolithic coupling in fluid–structure interaction with application to blood flow modeling”. In: *Journal of Computational Physics* 229.3 (2010), pp. 642–659. ISSN: 0021-9991. DOI: `https://doi.org/10.1016/j.jcp.2009.10.001`. URL: `http://www.sciencedirect.com/science/article/pii/S0021999109005464`.

[2] A Borghi et al. “Fluid–solid interaction simulation of flow and stress pattern in thoracoabdominal aneurysms: A patient-specific study”. In: *Journal of Fluids and Structures* 24.2 (2008), pp. 270–280. ISSN: 0889-9746. DOI: `https://doi.org/10.1016/j.jfluidstructs.2007.08.005`. URL: `http://www.sciencedirect.com/science/article/pii/S0889974607000709`.

[3] T H Webb and G M Williams. “Thoracoabdominal Aneurysm Repair”. In: *Cardiovascular Surgery* 7.6 (1999), pp. 573–585. DOI: `10.1177/096721099900700602`. URL: `https://doi.org/10.1177/096721099900700602`.

[4] John A Elefteriades. “Natural history of thoracic aortic aneurysms: indications for surgery, and surgical versus nonsurgical risks.” eng. In: *The Annals of thoracic surgery* 74.5 (Nov. 2002), pp. 1877–80. ISSN: 0003-4975 (Print).

[5] A T Culliford et al. “Aneurysms of the descending aorta. Surgical experience in 48 patients.” eng. In: *The Journal of thoracic and cardiovascular surgery* 85.1 (Jan. 1983), pp. 98–104. ISSN: 0022-5223 (Print).

[6] David A Vorp et al. “Effect of aneurysm on the tensile strength and biomechanical behavior of the ascending thoracic aorta.” eng. In: *The Annals of thoracic surgery* 75.4 (Apr. 2003), pp. 1210–1214. ISSN: 0003-4975 (Print).

[7] D. SHIELS, A. LEONARD, and A. ROSHKO. "FLOW-INDUCED VIBRATION OF A CIRCULAR CYLINDER AT LIMITING STRUCTURAL PARAMETERS". In: *Journal of Fluids and Structures* 15.1 (Jan. 2001), pp. 3–21. ISSN: 0889-9746. DOI: `10.1006/JFLS.2000.0330`. URL: `https://www.sciencedirect.com/science/article/pii/S088997460090330X`.

[8] C H K Williamson and R Govardhan. "VORTEX-INDUCED VIBRATIONS". In: *Annual Review of Fluid Mechanics* 36.1 (2004), pp. 413–455. DOI: `10.1146/annurev.fluid.36.050802.122128`. URL: `https://doi.org/10.1146/annurev.fluid.36.050802.122128`.

[9] Zhaolong Han et al. "Flow-induced vibrations of four circular cylinders with square arrangement at low Reynolds numbers". In: *Ocean Engineering* 96 (2015), pp. 21–33. ISSN: 0029-8018. DOI: `https://doi.org/10.1016/j.oceaneng.2014.12.002`. URL: `http://www.sciencedirect.com/science/article/pii/S002980181400451X`.

[10] Michael Paidoussis, Stuart J. Price, and Emmanuel de Langre. "Fluid-structure Interactions: Cross-flow-induced Instabilities". In: *Fluid-Structure Interactions: Cross-Flow-Induced Instabilities* (2010), pp. 1–402.

[11] A. Naseri et al. "SECOND-ORDER SEMI-IMPLICIT PARTITIONED METHOD FOR FLUID-STRUCTURE INTERACTION PROBLEMS". In: *6th European Conference on Computational Mechanics (ECCM 6)- 7th European Conference on Computational Fluid Dynamics (ECFD 7)*. 11-15 June. Glasgow, UK, 2018.

[12] Ahmad Amani et al. "A Study on Binary Collision of GNF Droplets Using a Conservative Level-Set Method". In: *6th European Conference on Computational Mechanics (ECCM 6)- 7th European Conference on Computational Fluid Dynamics (ECFD 7)*. Glasgow, UK, 2018.

[13] Joris Degroote. "Partitioned Simulation of Fluid-Structure Interaction". In: *Archives of Computational Methods in Engineering* 20.3 (Sept. 2013), pp. 185–238. ISSN: 1886-1784. DOI: `10.1007/s11831-013-9085-5`. URL: `https://doi.org/10.1007/s11831-013-9085-5`.

[14] Gene Hou, Jin Wang, and Anita Layton. “Numerical Methods for Fluid-Structure Interaction — A Review”. In: *Communications in Computational Physics* 12.2 (2012), 337–377. DOI: `10.4208/cicp.291210.290411s`.

[15] M Lesoinne and C Farhat. “Higher-Order Subiteration-Free Staggered Algorithm for Nonlinear Transient Aeroelastic Problems”. In: *AIAA Journal* 36.9 (Sept. 1998), pp. 1754–1757. ISSN: 0001-1452. DOI: `10.2514/2.7555`. URL: `https://doi.org/10.2514/2.7555`.

[16] Ulrich Küttler and Wolfgang A Wall. “Fixed-point fluid–structure interaction solvers with dynamic relaxation”. In: *Computational Mechanics* 43.1 (Dec. 2008), pp. 61–72. ISSN: 1432-0924. DOI: `10.1007/s00466-008-0255-5`. URL: `https://doi.org/10.1007/s00466-008-0255-5`.

[17] C Michler, E H van Brummelen, and R de Borst. “An interface Newton–Krylov solver for fluid–structure interaction”. In: *International Journal for Numerical Methods in Fluids* 47.10-11 (), pp. 1189–1195. DOI: `10.1002/fld.850`. URL: `https://onlinelibrary.wiley.com/doi/abs/10.1002/fld.850`.

[18] Miguel Ángel Fernández and Marwan Moubachir. “A Newton method using exact jacobians for solving fluid–structure coupling”. In: *Computers & Structures* 83.2 (2005), pp. 127–142. ISSN: 0045-7949. DOI: `https://doi.org/10.1016/j.compstruc.2004.04.021`. URL: `http://www.sciencedirect.com/science/article/pii/S0045794904002986`.

[19] Jean-Frédéric Gerbeau and Marina Vidrascu. “A Quasi-Newton Algorithm Based on a Reduced Model for Fluid-Structure Interaction Problems in Blood Flows”. In: *ESAIM: M2AN* 37.4 (2003), pp. 631–647. DOI: `10.1051/m2an:2003049`. URL: `https://doi.org/10.1051/m2an:2003049`.

[20] E H van Brummelen. “Added Mass Effects of Compressible and Incompressible Flows in Fluid-Structure Interaction”. In: *Journal of Applied Mechanics* 76.2 (Jan. 2009), pp. 21206–21207. ISSN: 0021-8936. URL: `http://dx.doi.org/10.1115/1.3059565`.

[21] P Causin, J F Gerbeau, and F Nobile. “Added-mass effect in the design of partitioned algorithms for fluid–structure problems”. In: *Computer Methods in Applied Mechanics and Engineering* 194.42 (2005), pp. 4506–4527. ISSN: 0045-7825. DOI: `https://doi.org/10.1016/j.cma.2004.12.005`. URL: `http://www.sciencedirect.com/science/article/pii/S0045782504005328`.

[22] Christiane Förster, Wolfgang A Wall, and Ekkehard Ramm. “Artificial added mass instabilities in sequential staggered coupling of nonlinear structures and incompressible viscous flows”. In: *Computer Methods in Applied Mechanics and Engineering* 196.7 (2007), pp. 1278–1293. ISSN: 0045-7825. DOI: `https://doi.org/10.1016/j.cma.2006.09.002`. URL: `http://www.sciencedirect.com/science/article/pii/S0045782506002544`.

[23] M Breuer and M Münsch. “Fluid-Structure Interaction Using LES - A Partitioned Coupled Predictor-Corrector Scheme”. In: *PAMM* 8.1 (), pp. 10515–10516. DOI: `10.1002/pamm.200810515`. URL: `https://onlinelibrary.wiley.com/doi/abs/10.1002/pamm.200810515`.

[24] Jón Tómas Grétarsson, Nipun Kwatra, and Ronald Fedkiw. “Numerically stable fluid–structure interactions between compressible flow and solid structures”. In: *Journal of Computational Physics* 230.8 (2011), pp. 3062–3084. ISSN: 0021-9991. DOI: `https://doi.org/10.1016/j.jcp.2011.01.005`. URL: `http://www.sciencedirect.com/science/article/pii/S0021999111000131`.

[25] M Astorino, F Chouly, and M Fernández. “Robin Based Semi-Implicit Coupling in Fluid-Structure Interaction: Stability Analysis and Numerics”. In: *SIAM Journal on Scientific Computing* 31.6 (2010), pp. 4041–4065. DOI: `10.1137/090749694`. URL: `https://doi.org/10.1137/090749694`.

[26] Tao He, Kai Zhang, and Tong Wang. “AC-CBS-Based Partitioned Semi-Implicit Coupling Algorithm for Fluid-Structure Interaction Using Stabilized Second-Order Pressure Scheme”. In: *Communications in Computational Physics* 21.5 (2017), 1449–1474. DOI: `10.4208/cicp.OA-2016-0106`.

[27] Alireza Naseri et al. “A semi-implicit coupling technique for fluid–structure interaction problems with strong added-mass effect”. In: *Journal of Fluids and Structures* 80 (2018), pp. 94–112. ISSN: 0889-9746. DOI: `https://doi.org/10.1016/j.jfluidstructs.2018.03.012`. URL: `http://www.sciencedirect.com/science/article/pii/S0889974617306886`.

[28] R P Chhabra and J F Richardson. “Non-Newtonian flow in the process industries : fundamentals and engineering applications”. In: (1999), pp. xiii, 436.

[29] J. F. Hutton H. A. Barnes and K. Walters. “An introduction to rheology”. In: *Polymer International* 25.1 (1989), p. 61. DOI: `10.1002/pi.4990250112`. URL: `https://onlinelibrary.wiley.com/doi/abs/10.1002/pi.4990250112`.

[30] Bird. *Transport Phenomena*.

[31] Pierre J Carreau. “Rheological Equations from Molecular Network Theories”. In: *Transactions of the Society of Rheology* 16.1 (1972), pp. 99–127. DOI: `10.1122/1.549276`. URL: `https://doi.org/10.1122/1.549276`.

[32] Srinivasa R Raghavan and Saad A Khan. “Shear-Thickening Response of Fumed Silica Suspensions under Steady and Oscillatory Shear”. In: *Journal of Colloid and Interface Science* 185.1 (1997), pp. 57–67. ISSN: 0021-9797. DOI: `https://doi.org/10.1006/jcis.1996.4581`. URL: `http://www.sciencedirect.com/science/article/pii/S0021979796945816`.

[33] R L Hoffman. “Discontinuous and dilatant viscosity behavior in concentrated suspensions. II. Theory and experimental tests”. In: *Journal of Colloid and Interface Science* 46.3 (1974), pp. 491–506. ISSN: 0021-9797. DOI: `https://doi.org/10.1016/0021-9797(74)90059-9`. URL: `http://www.sciencedirect.com/science/article/pii/0021979774900599`.

[34] G Bossis and J F Brady. “The rheology of Brownian suspensions”. In: *The Journal of Chemical Physics* 91.3 (1989), pp. 1866–1874. DOI: `10.1063/1.457091`. URL: `https://doi.org/10.1063/1.457091`.

[35] John F Brady and Georges Bossis. “The rheology of concentrated suspensions of spheres in simple shear flow by numerical simulation”. In: *Journal of Fluid Mechanics* 155 (1985), 105–129. DOI: `10.1017/S0022112085001732`.

[36] P N B Reis et al. “Impact response of Kevlar composites with filled epoxy matrix”. In: *Composite Structures* 94.12 (2012), pp. 3520–3528. ISSN: 0263-8223. DOI: `https://doi.org/10.1016/j.compstruct.2012.05.025`. URL: `http://www.sciencedirect.com/science/article/pii/S0263822312002516`.

[37] Abhijit Majumdar, Bhupendra Singh Butola, and Ankita Srivastava. “Development of soft composite materials with improved impact resistance using Kevlar fabric and nano-silica based shear thickening fluid”. In: *Materials & Design (1980-2015)* 54 (2014), pp. 295–300. ISSN: 0261-3069. DOI: `https://doi.org/10.1016/j.matdes.2013.07.086`. URL: `http://www.sciencedirect.com/science/article/pii/S0261306913007140`.

[38] Oren E Petel et al. “A comparison of the ballistic performance of shear thickening fluids based on particle strength and volume fraction”. In: *International Journal of Impact Engineering* 85 (2015), pp. 83–96. ISSN: 0734-743X. DOI: `https://doi.org/10.1016/j.ijimpeng.2015.06.004`. URL: `http://www.sciencedirect.com/science/article/pii/S0734743X15001207`.

[39] Robert J Rabb and Eric P Fahrenthold. “Evaluation of Shear-Thickening-Fluid Kevlar for Large-Fragment-Containment Applications”. In: *Journal of Aircraft* 48.1 (Jan. 2011), pp. 230–234. ISSN: 0021-8669. DOI: `10.2514/1.C031081`. URL: `https://doi.org/10.2514/1.C031081`.

[40] Ankita Srivastava, Abhijit Majumdar, and Bhupendra Singh Butola. “Improving the impact resistance performance of Kevlar fabrics using silica based shear thickening fluid”. In: *Materials Science and Engineering: A* 529 (2011), pp. 224–229. ISSN: 0921-5093. DOI: `https://doi.org/10.1016/j.msea.2011.09.021`. URL: `http://www.sciencedirect.com/science/article/pii/S0921509311009816`.

[41] Z H Tan et al. “Dynamic response of symmetrical and asymmetrical sandwich plates with shear thickening fluid core subjected to penetration loading”. In: *Materials & Design* 94 (2016), pp. 105–110. ISSN: 0264-1275. DOI: `https://doi.org/10.`

1016/j.matdes.2016.01.036. URL: http://www.sciencedirect.com/science/article/pii/S0264127516300375.

[42] Yurim Park et al. “Empirical study of the high velocity impact energy absorption characteristics of shear thickening fluid (STF) impregnated Kevlar fabric”. In: *International Journal of Impact Engineering* 72 (2014), pp. 67–74. ISSN: 0734-743X. DOI: https://doi.org/10.1016/j.ijimpeng.2014.05.007. URL: http://www.sciencedirect.com/science/article/pii/S0734743X14001146.

[43] Zhenqian Lu et al. “Compressive behaviors of warp-knitted spacer fabrics impregnated with shear thickening fluid”. In: *Composites Science and Technology* 88 (2013), pp. 184–189. ISSN: 0266-3538. DOI: https://doi.org/10.1016/j.compscitech.2013.09.004. URL: http://www.sciencedirect.com/science/article/pii/S0266353813003667.

[44] C Fischer et al. “Dynamic properties of sandwich structures with integrated shear-thickening fluids”. In: *Smart Materials and Structures* 15.5 (2006), p. 1467. URL: http://stacks.iop.org/0964-1726/15/i=5/a=036.

[45] Neil Sims, R Stanway, and A R. Johnson. “Vibration Control Using Smart Fluids: A State-of-the-Art Review”. In: *The Shock and Vibration Digest* 31 (1999), pp. 195–203.

[46] T G. Mezger. “The Rheology Handbook: For Users of Rotational and Oscillatory Rheometers”. In: *Vincentz Verlag* Hanover, G (2002), p. 299.

[47] Stanley Middleman. “Rheology: Principles, measurements, and applications by C. Macosko, VCH Publishers, 1994, 550pp., $95.00”. In: *AIChE Journal* 41.10 (), p. 2344. DOI: 10.1002/aic.690411025. URL: https://onlinelibrary.wiley.com/doi/abs/10.1002/aic.690411025.

[48] F. J. Galindo-Rosales, F. J. Rubio-Hernández, and A. Sevilla. “An apparent viscosity function for shear thickening fluids”. In: *Journal of Non-Newtonian Fluid Mechanics* 166.5-6 (2011), pp. 321–325. ISSN: 03770257. DOI: 10.1016/j.jnnfm.2011.01.001. URL: http://dx.doi.org/10.1016/j.jnnfm.2011.01.001.

[49] Todd M Squires and Stephen R Quake. "Microfluidics: Fluid physics at the nanoliter scale". In: *Rev. Mod. Phys.* 77.3 (Oct. 2005), pp. 977–1026. DOI: `10.1103/RevModPhys.77.977`. URL: `https://link.aps.org/doi/10.1103/RevModPhys.77.977`.

[50] Alex Groisman, Markus Enzelberger, and Stephen R Quake. "Microfluidic Memory and Control Devices". In: *Science* 300.5621 (2003), pp. 955–958. ISSN: 0036-8075. DOI: `10.1126/science.1083694`. URL: `http://science.sciencemag.org/content/300/5621/955`.

[51] Alex Groisman and Stephen R Quake. "A Microfluidic Rectifier: Anisotropic Flow Resistance at Low Reynolds Numbers". In: *Phys. Rev. Lett.* 92.9 (Mar. 2004), p. 94501. DOI: `10.1103/PhysRevLett.92.094501`. URL: `https://link.aps.org/doi/10.1103/PhysRevLett.92.094501`.

[52] Alexander N Morozov and Wim van Saarloos. "An introductory essay on subcritical instabilities and the transition to turbulence in visco-elastic parallel shear flows". In: *Physics Reports* 447.3 (2007), pp. 112–143. ISSN: 0370-1573. DOI: `https://doi.org/10.1016/j.physrep.2007.03.004`. URL: `http://www.sciencedirect.com/science/article/pii/S0370157307001469`.

[53] M J Crochet and M Bezy. "Numerical solution for the flow of viscoelastic fluids". In: *Journal of Non-Newtonian Fluid Mechanics* 5 (1979), pp. 201–218. ISSN: 0377-0257. DOI: `https://doi.org/10.1016/0377-0257(79)85014-4`. URL: `http://www.sciencedirect.com/science/article/pii/0377025779850144`.

[54] Robert E Gaidos and Ron Darby. "Numerical simulation and change in type in the developing flow of a nonlinear viscoelastic fluid". In: *Journal of Non-Newtonian Fluid Mechanics* 29 (1988), pp. 59–79. ISSN: 0377-0257. DOI: `https://doi.org/10.1016/0377-0257(88)85050-X`. URL: `http://www.sciencedirect.com/science/article/pii/037702578885050X`.

[55] S S Edussuriya, A J Williams, and C Bailey. "A cell-centred finite volume method for modelling viscoelastic flow". In: *Journal of Non-Newtonian Fluid Mechanics* 117.1 (2004), pp. 47–61. ISSN: 0377-0257. DOI: `https://doi.org/10.1016/`

j.jnnfm.2003.12.001. URL: http://www.sciencedirect.com/science/article/pii/S0377025703002593.

[56] J E López-Aguilar et al. “High-Weissenberg predictions for micellar fluids in contraction–expansion flows”. In: *Journal of Non-Newtonian Fluid Mechanics* 222 (2015), pp. 190–208. ISSN: 0377-0257. DOI: https://doi.org/10.1016/j.jnnfm.2014.11.008. URL: http://www.sciencedirect.com/science/article/pii/S0377025714002171.

[57] Y Kwon and A I Leonov. “Stability constraints in the formulation of viscoelastic constitutive equations”. In: *Journal of Non-Newtonian Fluid Mechanics* 58.1 (1995), pp. 25–46. ISSN: 0377-0257. DOI: https://doi.org/10.1016/0377-0257(94)01341-E. URL: http://www.sciencedirect.com/science/article/pii/037702579401341E.

[58] Antony N Beris and Kostas D Housiadas. “Computational Viscoelastic Fluid Mechanics and Numerical Studies of Turbulent Flows of Dilute Polymer Solutions”. In: *Modeling and Simulation in Polymers*. Wiley-Blackwell, 2010. Chap. 1, pp. 1–36. ISBN: 9783527324156. DOI: 10.1002/9783527630257.ch1. URL: https://onlinelibrary.wiley.com/doi/abs/10.1002/9783527630257.ch1.

[59] J. G. Oldroyd. “On the Formulation of Rheological Equations of State”. In: *Proceedings of the Royal Society A: Mathematical, Physical and Engineering Sciences* 200.1063 (1950), pp. 523–541. ISSN: 1364-5021. DOI: 10.1098/rspa.1950.0035. URL: http://rspa.royalsocietypublishing.org/cgi/doi/10.1098/rspa.1950.0035.

[60] H Giesekus. “A simple constitutive equation for polymer fluids based on the concept of deformation-dependent tensorial mobility”. In: *Journal of Non-Newtonian Fluid Mechanics* 11.1 (1982), pp. 69–109. ISSN: 0377-0257. DOI: https://doi.org/10.1016/0377-0257(82)85016-7. URL: http://www.sciencedirect.com/science/article/pii/0377025782850167.

[61] P A Stewart et al. “An Improved Sharp Interface Method for Viscoelastic and Viscous Two-Phase Flows”. In: *J. Sci. Comput.* 35.1 (Apr. 2008), pp. 43–61. ISSN: 0885-7474. DOI: 10.1007/s10915-007-9173-5. URL: http://dx.doi.org/10.1007/s10915-007-9173-5.

[62] Raanan Fattal and Raz Kupferman. “Constitutive laws for the matrix-logarithm of the conformation tensor”. In: *Journal of Non-Newtonian Fluid Mechanics* 123.2-3 (2004), pp. 281–285. ISSN: 03770257. DOI: 10.1016/j.jnnfm.2004.08.008.

[63] Nusret Balci et al. “Symmetric factorization of the conformation tensor in viscoelastic fluid models”. In: *Journal of Non-Newtonian Fluid Mechanics* 166.11 (2011), pp. 546–553. ISSN: 03770257. DOI: 10.1016/j.jnnfm.2011.02.008. URL: http://dx.doi.org/10.1016/j.jnnfm.2011.02.008.

[64] L. J. Amoreira and P. J. Oliveira. “Comparison of different formulations for the numerical calculation of unsteady incompressible viscoelastic fluid flow”. In: *Advances in Applied Mathematics and Mechanics* 2.4 (2010), pp. 483–502. ISSN: 20700733. DOI: 10.4208/aamm.10-m1010.

[65] Kausik Sarkar and William R. Schowalter. “Deformation of a two-dimensional viscoelastic drop at non-zero Reynolds number in time-periodic extensional flows”. In: *Journal of Non-Newtonian Fluid Mechanics* 95.2-3 (2000), pp. 315–342. ISSN: 03770257. DOI: 10.1016/S0377-0257(00)00156-7.

[66] A M Afonso, F T Pinho, and M A Alves. “The kernel-conformation constitutive laws”. In: *Journal of Non-Newtonian Fluid Mechanics* 167-168 (2012), pp. 30–37. ISSN: 0377-0257. DOI: https://doi.org/10.1016/j.jnnfm.2011.09.008. URL: http://www.sciencedirect.com/science/article/pii/S0377025711002370.

[67] X. Chen et al. “A comparison of stabilisation approaches for finite-volume simulation of viscoelastic fluid flow”. In: *International Journal of Computational Fluid Dynamics* 27.6-7 (2013), pp. 229–250. ISSN: 10618562 10290257. DOI: 10.1080/10618562.2013.829916.

[68] Oguz K Baskurt and Herbert J Meiselman. “Blood Rheology and Hemodynamics”. EN. In: *Semin Thromb Hemost* 29.05 (2003), pp. 435–450. ISSN: 0094-6176. DOI: 10.1055/s-2003-44551.

[69] Vittorio Cristini and Ghassan S Kassab. “Computer Modeling of Red Blood Cell Rheology in the Microcirculation: A Brief Overview”. In: *Annals of Biomedical Engineering* 33.12 (Dec. 2005), pp. 1724–1727. ISSN: 1573-9686. DOI: 10.1007/s10439-005-8776-y. URL: https://doi.org/10.1007/s10439-005-8776-y.

[70] Debadi Chakraborty and J Ravi Prakash. “Viscoelastic fluid flow in a 2D channel bounded above by a deformable finite-thickness elastic wall”. In: *Journal of Non-Newtonian Fluid Mechanics* 218.1 (2015), pp. 83–98. ISSN: 03770257. DOI: 10.1016/j.jnnfm.2015.02.003. URL: http://ac.els-cdn.com/S0377025715000282/1-s2.0-S0377025715000282-main.pdf?_tid=41aaaa18-6c79-11e7-8118-00000aacb35f&acdnat=1500465550_7257ca9a04716fae79ee052ca2e34769.

[71] Robert G Owens. “A new microstructure-based constitutive model for human blood”. In: *Journal of Non-Newtonian Fluid Mechanics* 140.1 (2006), pp. 57–70. ISSN: 0377-0257. DOI: https://doi.org/10.1016/j.jnnfm.2006.01.015. URL: http://www.sciencedirect.com/science/article/pii/S0377025706001480.

[72] M. Lukácova-Medvidova and A. Zaušková. “Numerical modelling of shear-thinning non-Newtonian flows in compliant vessels”. In: *International Journal for Numerical Methods in Fluids* 56.8 (2008), pp. 1409–1415. ISSN: 02712091. DOI: 10.1002/fld.1676.

[73] Xingyuan Chen, Michael Schäfer, and Dieter Bothe. “Numerical modeling and investigation of viscoelastic fluid-structure interaction applying an implicit partitioned coupling algorithm”. In: *Journal of Fluids and Structures* 54 (2015), pp. 390–421. ISSN: 10958622. DOI: 10.1016/j.jfluidstructs.2014.12.001. URL: http://dx.doi.org/10.1016/j.jfluidstructs.2014.12.001.

[74] Alexandre Joel Chorin. “Numerical solution of the Navier-Stokes equations”. In: *Mathematics of Computation* 22.104 (1968), pp. 745–745. ISSN: 0025-5718. DOI: 10.1090/S0025-5718-1968-0242392-2. URL: http://www.ams.org/jourcgi/jour-getitem?pii=S0025-5718-1968-0242392-2.

[75] O Estruch et al. “A parallel radial basis function interpolation method for unstructured dynamic meshes”. In: *Computers & Fluids* 80 (2013), pp. 44–54. ISSN: 0045-7930. DOI: `https://doi.org/10.1016/j.compfluid.2012.06.015`. URL: `http://www.sciencedirect.com/science/article/pii/S0045793012002381`.

[76] A. Amani et al. “A METHOD FOR FLUID-STRUCTURE INTERACTION PROBLEMS WITH NON-NEWTONIAN FLUID”. In: *6th European Conference on Computational Mechanics (ECCM 6)- 7th European Conference on Computational Fluid Dynamics (ECFD 7)*. 11-15 June. Glasgow, UK, 2018.

[77] Kerim Yapici, Bulent Karasozen, and Yusuf Uludag. “Journal of Non-Newtonian Fluid Mechanics Finite volume simulation of viscoelastic laminar flow in a lid-driven cavity”. In: 164 (2009), pp. 51–65. DOI: `10.1016/j.jnnfm.2009.08.004`.